

Neutrino signal dependence on gamma-ray burst emission mechanism

Tetyana Pitik,^a Irene Tamborra,^a and Maria Petropoulou^b

^aNiels Bohr International Academy and DARK, Niels Bohr Institute, University of Copenhagen, Blegdamsvej 17, 2100, Copenhagen

^bDepartment of Physics, National and Kapodistrian University of Athens, Panepistimiopolis, 15783 Zografos, Greece

E-mail: tetyana.pitik@nbi.ku.dk, tamborra@nbi.ku.dk, mpetropo@phys.uoa.gr

Abstract. Long duration gamma-ray bursts (GRBs) are among the least understood astrophysical transients powering the high-energy universe. To date, various mechanisms have been proposed to explain the observed electromagnetic GRB emission. In this work, we show that, although different jet models may be equally successful in fitting the observed electromagnetic spectral energy distributions, the neutrino production strongly depends on the adopted emission and dissipation model. To this purpose, we compute the neutrino production for a benchmark high-luminosity GRB in the internal shock model, including a dissipative photosphere as well as three emission components, in the jet model invoking internal-collision-induced magnetic reconnection and turbulence (ICMART), in the case of a magnetic jet with gradual dissipation, and in a jet with dominant proton synchrotron radiation. We find that the expected neutrino fluence can vary up to 1–1.5 orders of magnitude in amplitude and peak at energies ranging from 10^4 to 10^8 GeV. For our benchmark input parameters, none of the explored GRB models is excluded by the targeted searches carried out by the IceCube and ANTARES Collaborations. However, our work highlights the potential of high-energy neutrinos of pinpointing the underlying GRB emission mechanism and the importance of relying on different jet models for unbiased stacking searches.

Contents

1	Introduction	2
2	Dynamical evolution of gamma-ray burst jets	3
2.1	Kinetic dominated jets	4
2.1.1	Jet model with internal shocks	6
2.1.2	Jet model with a dissipative photosphere and internal shocks	7
2.1.3	Jet model with three emission components	7
2.2	Poynting flux dominated jets	8
2.2.1	ICMART model	8
2.2.2	Magnetized jet model with gradual dissipation	9
2.3	Proton synchrotron model	11
3	Main model ingredients	11
3.1	Reference model parameters	11
3.2	Spectral energy distribution of protons	13
4	Neutrino production in the gamma-ray burst jet	14
5	Results: Gamma-ray burst neutrino emission	16
5.1	Kinetic dominated jets	16
5.1.1	Jet model with internal shocks	16
5.1.2	Jet model with a dissipative photosphere and internal shocks	17
5.1.3	Jet model with three emission components	19
5.2	Poynting flux dominated jets	22
5.2.1	ICMART model	22
5.2.2	Magnetized jet model with gradual dissipation	23
5.3	Proton synchrotron model	25
6	Discussion	28
6.1	Energetics	28
6.2	Detection perspectives	29
7	Conclusions	31
A	Spectral energy distributions of photons: fitting functions	31
A.1	Band function	32
A.2	Cut-off power-law	32
A.3	Power law	33
A.4	Double broken power law	33
B	Magnetized jet model with gradual dissipation: dependence of the neutrino emission on the input parameters	33

1 Introduction

Gamma-ray bursts (GRBs) are irregular pulses of gamma-rays that have puzzled astronomers for a long time [1]. Exhibiting a non-thermal spectrum, typically peaking in $10\text{--}10^4$ keV energy band [2], bursts lasting for more than 2 s are named long-duration GRBs and are thought to be harbored within collapsing massive stars [3–5]. They are the brightest explosions in our universe and can release isotropic energies as high as 10^{54} erg in gamma-rays over few tens of seconds [6].

The central engine of a long-duration GRB jet can either be a hyper-accreting black hole or a rapidly spinning magnetar. Because the central engine cannot be directly observed, its nature can be inferred only indirectly through its impact on the electromagnetic properties of GRBs (see, e.g., Ref. [7] and references therein). A bipolar outflow is continuously powered for a certain time interval, during which gravitational energy [8, 9] (for accreting systems) or spin energy [10, 11] (for spinning-down systems) is released in the form of thermal energy or Poynting flux energy, respectively. Subsequently, the outflow propagates through the star and it is strongly collimated by the stellar envelope. Once it succeeds to break out of the stellar surface, it manifests itself as the jet responsible for the GRBs that we observe at Earth. The dynamical evolution of the jet strongly depends on the initial conditions of the central engine. If the magnetic field is negligible, the evolution of the outflow can be well described by the fireball model [12]. If instead the central engine harbours a strong magnetic field, the jet dynamics is significantly different [13].

Gamma-ray bursts are candidate sources of ultra-high energy cosmic rays and high energy neutrinos [14]. In the prompt phase, if the jet contains baryons, protons and nuclei are expected to be accelerated [15]. If a photon field is also present, photo-hadronic ($p\gamma$) interactions can lead to a significant flux of neutrinos [16–18]. Another copious source of neutrinos comes from hadronic collisions (pp or pn) which, however, are most efficient inside the progenitor star where the baryon density is large [15, 19–21]. Given the typical GRB parameters, neutrinos produced in the optically thin region are expected to be emitted in the TeV–PeV energy range [16, 22–24].

The IceCube Neutrino Observatory routinely detects neutrinos of astrophysical origin in the TeV–PeV energy range [25–28]. However, despite the fact that several sources have been proposed as possible candidates to explain the neutrino flux that we observe [22–24, 29, 30], we are still lacking clear evidence on the sources producing the observed neutrinos. Among the candidate sources, high-luminosity GRBs are deemed to be responsible for less than 10% of the observed diffuse emission in the TeV energy range [27, 31]. On the other hand, over the years, the IceCube and ANTARES Collaborations have searched for high-energy neutrinos emitted in coincidence with GRBs observed by the Fermi satellite [31–33], gradually placing more stringent upper limits on somewhat optimistic GRB emission models. Recent work suggests that current limits are still not stringent enough to rule out more realistic estimations proposed in the literature [15, 34–38].

Intriguingly, besides the need for increased detection sensitivity, one of the reasons for the non-detection of GRB neutrinos could be connected to the theoretical modeling of the neutrino emission, which is strictly linked to the electromagnetic modeling of the jet. In fact, a comprehensive explanation of the GRB emission and dissipation mechanism is still lacking due to the failure of existing models in addressing all observations in the spectral and temporal domains.

On the other hand, the scarce amount of data on high energy photons and the related

statistical challenges allow for a certain flexibility in fitting the same set of data with different input models for GRBs—see, e.g., Refs. [39–43].

Different GRB models may lead to very different predictions for the neutrino emission. The latter depends on the target photon spectrum and the properties of the accelerated proton distribution (i.e., energy density, power-law slope, and maximum energy), both depending on the emission and dissipation mechanisms as well as the location of the proton acceleration region.

In this work, we compute the neutrino emission for a benchmark high-luminosity GRB in various jet emission and dissipation scenarios. In particular, we consider an internal shock (IS) model [44], a dissipative photosphere model in the presence of ISs (PH-IS) [45], a three-component model (3-COMP) with emission arising from the photosphere, the IS, and external shock [46], and the internal-collision-induced magnetic reconnection and turbulence model (ICMART) [47]. We also compute, for the first time, the neutrino signal expected in two models where the jet is assumed to be magnetically dominated, namely a magnetized jet model with gradual dissipation (MAG-DISS) [48, 49], and a proton synchrotron emission model (p-SYNCH) [50]. Our goal is to make a fair comparison among the proposed models for dissipation and electromagnetic emission in GRBs for what concerns the expected neutrino signal.

This paper is organized as follows. In Sec. 2, we outline the basics of the dynamical evolution of the GRB jets considered in this paper. The main model ingredients as well as the proton energy distributions are reported in Sec. 3. The neutrino production mechanism is discussed in Sec. 4. The neutrino emission is presented in Sec. 5, first in various scenarios involving ISs, then in the case of magnetized jets, and lastly for the proton synchrotron mechanism. A discussion on our findings, also in the context of detection perspectives, and conclusions are reported in Secs. 6 and 7, respectively. The fitting functions adopted for the photon spectral energy distributions are listed in Appendix A. A discussion on the dependence of the neutrino emission on the input parameters for the magnetic model with gradual dissipation is reported in Appendix B.

2 Dynamical evolution of gamma-ray burst jets

In this section, we introduce the main physics describing the jet models considered in this work. We present the models in the context of kinetic dominated jets, then focus on two cases of Poynting flux dominated jets, and the proton synchrotron model. Note that, despite the fact that the proton synchrotron model has a Poynting luminosity larger than the kinetic one (see Ref. [51] for a dedicated discussion), we treat it separately from the Poynting flux dominated jets because it does not require knowledge of the jet dynamics.

The general GRB model envisages a relativistic jet propagating with Lorentz factor Γ , with respect to the central engine frame, and half opening angle θ_j . As long as $\Gamma^{-1} < \theta_j$, which is expected to hold during the prompt phase [52], the radiating region can be considered spherically symmetric. We therefore use isotropic equivalent quantities throughout the paper.

The reference frames used in our calculation are the observer frame (on Earth), the frame of the central engine (laboratory frame), and the jet comoving frame. A quantity characteristic of the jet is labeled as X , \tilde{X} , and X' , in each of these frames, respectively. For example, energy is transformed through the following relation: $\tilde{E} = (1+z)E = (1+z)\mathcal{D}E'$; time instead transforms as $t = (1+z)\tilde{t} = (1+z)\mathcal{D}^{-1}t'$, with $\mathcal{D} = [\Gamma(1 - \beta \cos \theta)]^{-1}$ being the Doppler factor, $\beta = v/c$, $\Gamma = 1/\sqrt{1 - \beta^2}$ the Lorentz boost factor and θ the angle of

propagation of an ejecta element with respect to the line of sight. A characteristic quantity of the jet is the isotropic-equivalent energy, \tilde{E}_{iso} , which represents the energetic content of the outflow and it is related to the bolometric energy \tilde{E}_{bol} through the opening angle by the following relation: $\tilde{E}_{\text{bol}} = (1 - \cos \theta_j) \tilde{E}_{\text{iso}} \approx (\theta_j^2/2) \tilde{E}_{\text{iso}}$, where the approximation holds for small opening angles.

The dominant source of energy in a GRB jet is related to the initial conditions. The jet is powered by accretion onto a newly formed black hole [3] or a rapidly spinning massive neutron star [11]. Two mechanisms are invoked to extract energy from the central compact object and power the GRB jet: neutrino annihilation [8, 53, 54] or the extraction of magnetic energy at the expenses of the central object spin energy [10, 55].

2.1 Kinetic dominated jets

We start with the case of a generic fireball composed of photons, electron/positron pairs, and a small fraction of baryons (primarily protons and neutrons), with negligible magnetic fields [56, 57]. The dynamical evolution of the fireball is sketched in Fig. 1 and consists of three phases, namely acceleration, coasting, and deceleration:

1. *Fireball acceleration:* A hot relativistic fireball of isotropic energy $\tilde{E}_{\text{iso}} = \tilde{L}_{\text{iso}} \tilde{t}_{\text{dur}}$ is created and launched at the radius R_0 by the central engine emitting energy with luminosity \tilde{L}_{iso} for a time \tilde{t}_{dur} . Since after the propagation through the envelope of

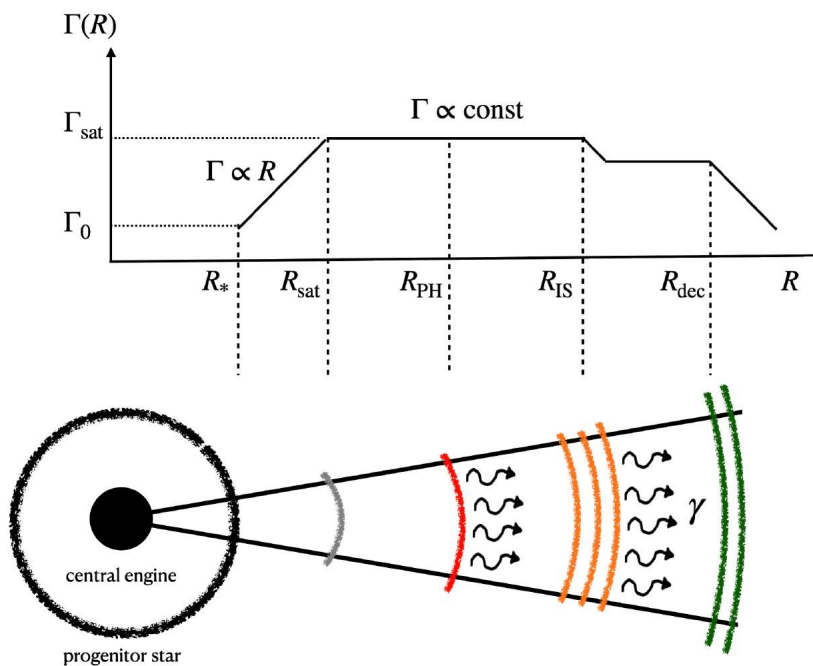


Figure 1. Schematic representation of a GRB jet (not in scale) where energy dissipation takes place through relativistic shocks. The Lorentz factor Γ is shown as a function of the fireball radius for the case in which the photosphere occurs in the coasting phase, so that the photospheric radius (R_{PH}) lies above the saturation radius (R_{sat}). The photosphere is assumed to produce thermal γ -rays, the ISs forming at R_{IS} are thought to produce non-thermal γ -rays, and the external shock, which starts to decelerate at R_{dec} , is responsible for the afterglow. When energy dissipation takes place below the photosphere, non-thermal radiation is also expected from R_{PH} .

the progenitor star, the fireball can be re-born [58], we adopt as size of the jet base $R_0 = R_\star \theta_j$, with $R_\star \simeq 10^{11}$ cm being the progenitor star radius. The width of the emitted shell is $\tilde{\Delta} = c\tilde{t}_{\text{dur}}$. As the fireball shell undergoes adiabatic expansion, and while the pair plasma retains relativistic temperatures, baryons are accelerated by radiation pressure and the bulk Lorentz factor increases linearly with radius ($\Gamma \propto R$), until it reaches its maximum value. We assume that the latter coincides with the dimensionless entropy per baryon $\eta = \tilde{E}_{\text{iso}}/Mc^2$, where M is the baryonic mass injected into the outflow. The maximum Lorentz factor is achieved at the saturation radius $R_{\text{sat}} = \eta R_0$.

2. *Fireball coasting*: Beyond R_{sat} , the flow coasts with $\Gamma = \Gamma_{\text{sat}} \sim \eta = \text{const}$. As the fireball shell keeps on expanding, the baryon density, obtained by the mass continuity equation $\dot{M} = 4\pi R^2 \Gamma \rho' c = \text{const}$ [59] for a relativistic flow with spherical symmetry, drops as

$$n'_b = \frac{\rho'}{m_p} = \frac{\dot{M}}{4\pi m_p R^2 c \Gamma} \simeq \frac{\tilde{L}_{\text{iso}}}{4\pi R^2 m_p c^3 \eta \Gamma}, \quad (2.1)$$

where ρ' is the baryon density in the comoving frame, R is the distance from the central engine, and $\tilde{L}_{\text{iso}} = \eta \dot{M} c^2$. At a certain point, photons become optically thin to both pair production and Compton scattering off free leptons associated with baryons entrained in the fireball. Once the Thomson optical depth ($\tau_T = n'_l \sigma_T R / \Gamma$) drops below 1, the energy that has not been converted into kinetic energy is released at the photospheric radius R_{PH} . Let \mathcal{R} denote the number of leptons per baryon ($n'_l = \mathcal{R} n'_p$), we can define the critical dimensionless entropy [60]:

$$\eta_* = \left(\frac{\sigma_T \mathcal{R} \tilde{L}_{\text{iso}} \Gamma_0}{8\pi R_0 m_p c^3} \right)^{1/4}, \quad (2.2)$$

where $\sigma_T = 6.65 \times 10^{-25} \text{cm}^2$ is the Thomson cross section, and $\Gamma_0 = \Gamma(R_\star) \simeq 1\text{--}10$ [61] is the breakout Lorentz factor. η_* represents the limiting value of the Lorentz factor which separates two scenarios: $\eta > \eta_*$ (the photosphere occurs in the acceleration phase) and $\eta < \eta_*$ (the photosphere occurs in the coasting phase). For our choice of parameters, we will always be in the second case, thus we can introduce the photospheric radius as the distance such that $\tau_T = 1$ [62]:

$$R_{\text{PH}} = \frac{\sigma_T \tilde{L}_{\text{iso}} \mathcal{R}}{4\pi \eta^3 m_p c^3}. \quad (2.3)$$

The radiation coming from the photosphere is the first electromagnetic signal detectable from the fireball. It emerges peaking at [62]

$$k_B \tilde{T}_{\text{PH}} = k_B \left(\frac{\tilde{L}_{\text{iso}}}{4\pi R_0^2 \sigma_B} \right)^{1/4} \left(\frac{R_{\text{PH}}}{R_{\text{sat}}} \right)^{-2/3}, \quad (2.4)$$

where σ_B is the Stefan-Boltzmann constant and k_B the Boltzmann constant. The energy \tilde{E}_{PH} emerging from the photosphere is parametrized through $\varepsilon_{\text{PH}} = \tilde{E}_{\text{PH}}/\tilde{E}_{\text{iso}}$. Since the central engine responsible for the launch of the relativistic jet is expected to have an erratic activity, the produced outflow is unsteady and radially inhomogeneous.

This causes internal collisions between shells of matter emitted with time lag t_v to occur at a distance [44]

$$R_{\text{IS}} \simeq \frac{2ct_v\Gamma^2}{1+z} ; \quad (2.5)$$

this is the IS radius, where a fraction ε_{IS} of the total outflow energy (\tilde{E}_{iso}) is dissipated, and particles are accelerated.

3. *Fireball deceleration*: The fireball shell is eventually decelerated [57, 63, 64] by the circumburst medium that can either be the interstellar medium or the pre-ejected stellar wind from the progenitor before the collapse. Let us consider an external density profile [65]:

$$n_b(R) = AR^{-s} , \quad (2.6)$$

with $s = 0$ for a homogeneous medium and $s = 2$ for a wind ejected at constant speed. For a thin shell [66], the deceleration radius is defined as the distance where the swept mass from the circumburst medium is $m_{\text{CMB}} = M/\eta$ [or $\Gamma(R_{\text{dec}}) = \eta/2$] [67]:

$$R_{\text{dec}} = \left(\frac{3-s}{4\pi} \frac{\tilde{E}_{\text{K,iso}}}{m_p c^2 A \eta^2} \right)^{1/(3-s)} ; \quad (2.7)$$

in alternative, R_{dec} can be obtained from the observed deceleration time t_{dec} [68]:

$$t_{\text{dec}} \simeq 1.3(1+z) \frac{R_{\text{dec}}}{\eta^2 c} , \quad (2.8)$$

where $\tilde{E}_{\text{K,iso}} = \tilde{E}_{\text{iso}} - \tilde{E}_{\gamma,\text{iso}}$ is the isotropic equivalent kinetic energy of the outflow after $\tilde{E}_{\gamma,\text{iso}}$ has been radiated during the prompt phase. At R_{dec} , an external shock forms and propagates into the medium, hence the deceleration radius is essentially the initial external shock radius.

2.1.1 Jet model with internal shocks

For long time, the IS model [44, 69, 70] has been considered as the standard model for the prompt emission in the literature. Among the merits of this model there is its ability to naturally explain the variability of the lightcurves, to provide natural sites for the dissipation of the kinetic energy of the baryonic fireball, as well as sites for particle acceleration and non-thermal radiation.

The erratic activity of the central engine is responsible for the creation of an outflow that can be visualized as being composed of several shells. Collisions of such shells with different masses and/or Lorentz factors cause the dissipation of the kinetic energy of the jet at R_{IS}^1 (see Fig. 1).

Part of the dissipated energy, $\varepsilon_{\text{IS}}\tilde{E}_{\text{iso}}$, is used for particle acceleration. Non-thermal electrons (protons) receive a fraction ε_e (ε_p), while the magnetic field receives a fraction ε_B of that energy. In this scenario, electrons emit synchrotron radiation in the fast cooling regime. The radiated energy can thus be expressed as $E'_{\gamma,\text{iso}} = \varepsilon_e \varepsilon_{\text{IS}} E'_{\text{iso}}$ and the magnetic field as

$$B' = \sqrt{8\pi \frac{\varepsilon_B}{\varepsilon_e} \frac{E'_{\gamma,\text{iso}}}{V'_{\text{iso}}}} . \quad (2.9)$$

¹If there is a large spread in the Γ values of the shells, then R_{IS} can also spread a lot [71–73].

The protons co-accelerated with electrons interact with the prompt photons through photo-hadronic interactions and produce neutrinos, as discussed in Sec. 4. Here $V'_{\text{iso}} = 4\pi R_{\gamma}^2 \Gamma \tilde{c} t_{\text{dur}}$ represents the isotropic volume of the jet in the comoving frame.

Within a more realistic setup, various collisions between plasma shells occur along the jet. Scenarios involving collisions of multiple shells have been considered [71–73] and can lead to lower neutrino fluxes. Yet, in this work, since we aim to compare different jet models, we adopt one representative shell with average parameters and spectral properties for simplicity.

2.1.2 Jet model with a dissipative photosphere and internal shocks

In the class of photospheric models, it is assumed that the dominant radiation observed in the prompt phase is produced in the optically thick region below the photosphere [74]. Depending on the presence of dissipative processes acting in the optically thick parts of the outflow, photospheric models can be classified in non-dissipative or dissipative ones.

In the presence of a non-dissipative photosphere, according to the standard fireball model, the thermal radiation advected with the flow and unaffected by the propagation is released at R_{PH} , see Fig. 1. Depending on the dimensionless entropy of the outflow (see Eq. 2.2), this component can be very bright or highly inefficient and is characterized by the fraction $\varepsilon_{\text{PH}} = (\eta/\eta_*)^{8/3}$ [62].

For a dissipative photosphere, strong subphotospheric dissipation is required in the optically thick inner parts of relativistic outflows in order to account for the detected non-thermal spectra [75–81]. In this scenario, the spectral peak and the low-energy spectrum below the peak are formed by quasi-thermal Comptonization of seed photons by mildly relativistic electrons when the Thomson optical depth of the flow is $1 \lesssim \tau_T \lesssim 100$ [82, 83]. In the literature, several sub-photospheric dissipative mechanisms have been proposed, including ISs at small-radii [78], collisional nuclear processes [84], or dissipation of magnetic energy [82]. One of the most attractive features of these models is their ability to naturally explain the observed small dispersion of the sub-MeV peak and the high prompt emission efficiency [58, 85, 86], that the standard version of the IS model cannot easily explain.

The scenario explored in this work considers the main prompt emission as being released at R_{PH} with a non-thermal spectrum. These photons cross the IS region and interact with energetic protons accelerated at the IS to produce neutrinos. We do not consider neutrino production below and at the photosphere, as this would result in neutrino energies well below the PeV range that we are interested in (i.e., GeV neutrinos produced in proton-neutron collisions in the ejecta [87, 88] or TeV neutrinos produced via pp interactions of protons accelerated at sub-photospheric ISs [20, 89–92]). Indeed, photo-hadronic interactions in the opaque region do not lead to efficient production of high-energy neutrinos because of inefficient Fermi acceleration that limits the maximum proton energy to low values [93].

2.1.3 Jet model with three emission components

The three-component GRB model was introduced in Ref. [46], where the authors found that a thermal component described by a black body (BB) spectrum, a Band spectrum (sometimes statistically equivalent to a cut-off power-law, CPL) and a non-thermal power-law (PL) spectrum at high energies (with or without cut-off) represent a globally better description of the data than the Band spectral fit for a number of bursts. We refer the reader to Appendix A for details on the spectral energy distributions of photons.

As argued in Ref. [46], the physical interpretation proposed for the three components is the following. The BB component, given its weakness, is interpreted as thermal photospheric

emission of a magnetized jet not strongly affected by sub-photospheric dissipation. The non-thermal emission fitted by the Band (or CPL) component, given the observed variability, is assumed to be produced in the optically thin region of the jet from relativistic electrons. The third PL (or CPL) component, which extends over at least 5 decades in energy and sometimes emerges with a slight temporal delay with respect to the trigger of the burst, is the one with the least clear origin. Because of its initial temporal variability, it is assumed to be of internal origin; e.g., it might be due to inverse Compton processes, even if this scenario is not able to explain the extension of such a component to lower energies or the temporal delay. Finally, the fact that in some cases the PL component becomes dominant at the end of the bursts and lasts longer than the prompt emission led to identify it with the emergence of an early afterglow, which corresponds to the start of deceleration of the outflow.

2.2 Poynting flux dominated jets

When the central compact object is a rapidly rotating black hole threaded by open magnetic field lines, it is possible to tap the black hole spin energy to produce Poynting-flux dominated jets [10]. The electromagnetic luminosity of this jet is much larger than the kinetic luminosity associated to matter.

A characteristic parameter is the magnetization σ , defined as the ratio of the Poynting luminosity and the kinetic luminosity:

$$\sigma(R) \equiv \frac{L_B}{L_K} = \frac{B^2(R)}{4\pi\Gamma\rho(R)c^2} = \frac{B'^2(R)}{4\pi\rho'(R)c^2}, \quad (2.10)$$

where $B'(R)$ and $\rho'(R)$ are the magnetic field strength and matter density in the comoving frame at a certain distance R from the central engine. Hence, the total jet luminosity at any radius is $L(R) = [1 + \sigma(R)]L_K(R)$. In this work we consider two models for magnetized jets: the ICMART model and the gradual magnetic dissipation model, which we briefly introduce below.

2.2.1 ICMART model

The ICMART model [47] considers Poynting flux dominated jets, whose energy is dissipated and radiated away at very large radii from the central engine, as shown in Fig. 2. The main motivation behind this model relies on the non-detection (or detection of a very weak) photospheric component in the spectra of some GRBs, hinting that the jet composition cannot be largely Poynting flux dominated at the photosphere.

The GRB central engine intermittently ejects an unsteady jet with variable Lorentz factor and with a nearly constant degree of magnetization $\sigma_0 \equiv \sigma(R_0)$. Such a jet is composed by many discrete magnetized shells which collide at R_{IS} (see Eq. 2.5 and Fig. 2). Yet, the kinetic energy dissipated at the ISs is smaller by a factor $[1 + \sigma(R_{\text{IS}})]$ with respect to the energy available in the traditional IS model. Hence, the total energy emitted in radiation could be completely negligible at this stage.

In the optically thin region, the early internal collisions have the role of altering, and eventually destroying, the ordered magnetic field configuration, triggering the first reconnection event. The ejection of plasma from the reconnection layer would disturb the nearby ambient plasma and produce turbulence, facilitating more reconnection events which would lead to a runaway catastrophic release of the stored magnetic field energy at the radius defined as R_{ICMART} . This would correspond to one ICMART event, which would compose one

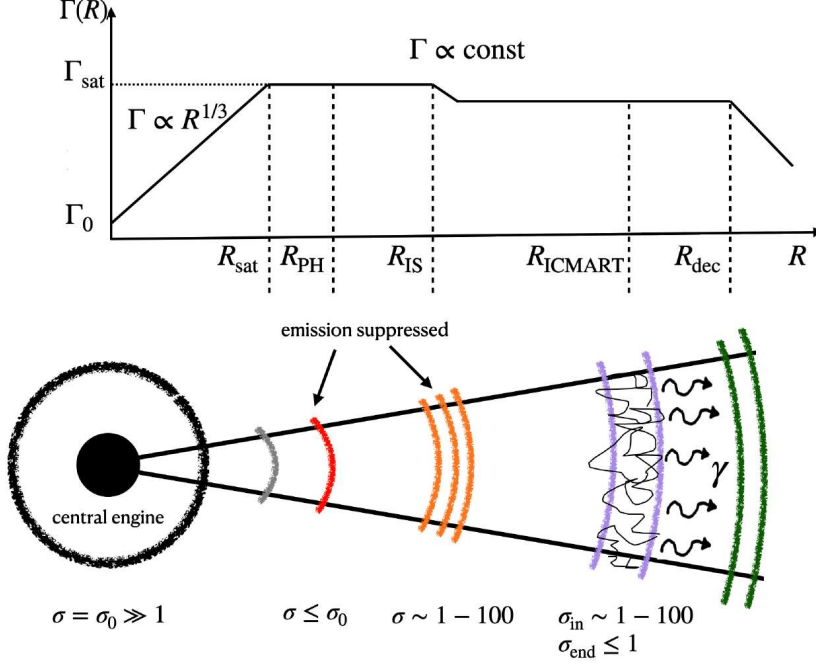


Figure 2. Schematic representation of a Poynting flux dominated jet (not in scale) in the ICMART model. The Lorentz factor Γ is shown as a function of jet radius. The radiation from the photosphere (R_{PH}) and ISs (R_{IS}) is strongly suppressed and can be at most $1/(\sigma + 1)$ of the total jet energy (see Eq. 2.10); typical values for the magnetization parameter σ are shown. The emitting region is located at R_{ICMART} , where magnetic reconnection causes a strong discharge of magnetic energy and the emission of gamma-rays. The magnetization at R_{ICMART} is σ_{in} and σ_{end} in the beginning and at the end of an ICMART event, respectively.

GRB pulse. Other collisions that trigger other reconnection-turbulence avalanches would give rise to other pulses.

This model successfully reproduces the observed GRB lightcurves with both fast and slow components [94]. The slow component, related to the central engine activity, would be caused by the superposition of emission from all the mini-jets due to multiple reconnection sites, while the erratic fast component would be related to the mini-jets pointing towards the observer.

2.2.2 Magnetized jet model with gradual dissipation

In this scenario, significant magnetic dissipation already occurs below the jet photosphere, as schematically shown in Fig. 3. Following Refs. [48, 49], we consider magnetized outflows with a striped-wind magnetic field structure, where energy is gradually dissipated through magnetic reconnection until the saturation radius. This model can naturally explain the double-hump electromagnetic spectra sometimes observed [49].

The jet is injected at $R_0 \sim 10^7$ cm with magnetization $\sigma_0 \gg 1$ and Lorentz factor $\Gamma_0 = \sqrt{\sigma_0 + 1} \approx \sigma_0$. As it propagates, the magnetic field lines of opposite polarity reconnect, causing the magnetic energy to be dissipated at a rate:

$$\dot{E}_{\text{diss}} = -\frac{dL_B}{dR} = -\frac{d}{dR} \left(\frac{\sigma}{\sigma + 1} L \right) \propto R^{1/3}, \quad (2.11)$$

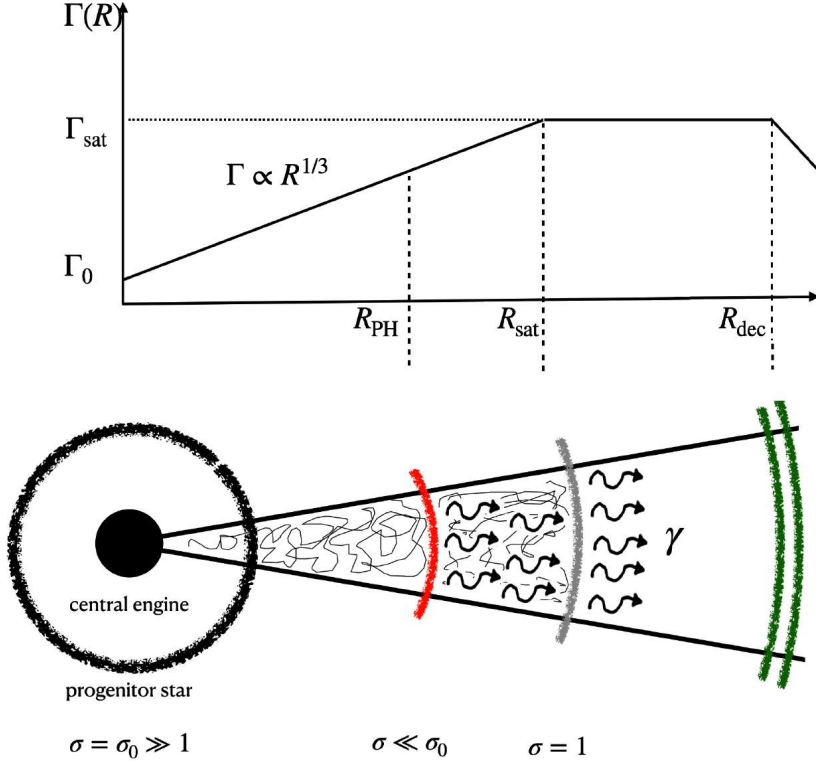


Figure 3. Schematic representation of a Poynting flux dominated jet (not in scale) in the gradual energy dissipation model. The Lorentz factor Γ is shown as a function of jet radius. The radiation from the photosphere (R_{PH}) can be very bright, depending on the initial magnetization σ_0 of the outflow. Typical values for the magnetization parameter σ are shown. The emitting region is located between R_{PH} and R_{sat} , where magnetic reconnection causes the dissipation of magnetic field energy, the emission of thermal gamma-rays at R_{PH} and synchrotron radiation from accelerated electrons in the optically thin region up to R_{sat} .

where $\sigma(R)$ is obtained from the conservation of the total specific energy $\Gamma(R)\sigma(R) = \Gamma_0\sigma_0$. The Lorentz factor of the flow evolves as

$$\Gamma(R) = \Gamma_{\text{sat}} \left(\frac{R}{R_{\text{sat}}} \right)^{1/3}, \quad (2.12)$$

until the saturation radius $R_{\text{sat}} = \lambda\Gamma_{\text{sat}}^2$ (see Fig. 3), where λ is connected to the characteristic length scale over which the magnetic field lines reverse polarity. This length scale can be related to the angular frequency of the central engine (e.g., of millisecond magnetars) or with the size of the magnetic loops threading the accretion disk [95].

Motivated by results of particle-in-cell (PIC) simulations of magnetic reconnection in magnetically dominated electron-proton plasmas [96–98], we assume that half of the dissipated energy in Eq. 2.11 is converted in kinetic energy of the jet, while the other half goes into particle acceleration and is redistributed among electrons and protons². In particular,

²Rough energy equipartition between magnetic field, protons and electron-positron pairs is also found in kinetic simulations of reconnection in pair-proton plasmas [99].

the fraction of energy which goes into electrons is [98]

$$\varepsilon_e \approx \frac{1}{4} \left(1 + \sqrt{\frac{\sigma}{10 + \sigma}} \right), \quad (2.13)$$

while the one that goes into protons has been extracted from Fig. 20 of Ref. [98] and is $\varepsilon_p \sim 1 - \varepsilon_e$. A fraction ξ of electrons injected into the dissipation region are accelerated into a power-law distribution $n'_e(\gamma'_e) \propto \gamma'^{-k_e}$ in the interval $[\gamma'_{e,\min}, \gamma'_{e,\max}]$ with the minimum electron Lorentz factor being

$$\gamma'_{e,\min}(R) = \frac{k_e - 2}{k_e - 1} \frac{\varepsilon_e}{2\xi} \sigma(R) \frac{m_p}{m_e}, \quad (2.14)$$

and $\gamma'_{e,\max}$ is the maximum electron energy obtained by equating the acceleration time and the total cooling time. The power-law slope of the accelerated particles in relativistic reconnection depends on the plasma magnetization in a way that harder spectra ($k_e < 2$) are obtained for $\sigma \gg 1$ [100–102]. Here, we adopt the following parameterization for the electron power-law slope [98]:

$$k_e(\sigma) \approx 1.9 + 0.7\sqrt{\sigma}. \quad (2.15)$$

The proton spectrum will be discussed in detail in Sec. 5.2.2.

2.3 Proton synchrotron model

Recently, Refs. [39, 103, 104] have analyzed the spectra of a sample of GRBs for which data down to the soft X-ray band and, in some cases, in the optical are available. This extensive work has established the common presence of a spectral break in the low energy tail of the prompt spectra and led to realize that the spectra could be fitted by three power-laws. The spectral indices below and above the break are found to be $\alpha_1 \simeq -2/3$ and $\alpha_2 \simeq -3/2$ respectively, while the photon index of the third PL is $\beta < 2$. The values of all photon indexes are consistent with the predicted values for the synchrotron emission in a marginally fast cooling regime [105]. However, if electrons are responsible for the prompt emission, then the parameters of the jet have to change drastically with respect to the standard scenario, in which the emission takes place at relatively small radii and with strong magnetic fields in situ. One possible way out to this has been discussed in Ref. [50], where protons are considered to be the particles which radiate synchrotron emission in the marginally fast cooling regime; in this way, it is possible to recover the typical emitting region size at $R_\gamma \simeq 10^{13}$ cm.

3 Main model ingredients

In this section, we outline some of the quantities characterizing the energetics and geometry of the jet for all models. We also introduce the target particle distributions.

3.1 Reference model parameters

The gamma-ray emission is assumed to originate from an isotropic volume $V'_{\text{iso},s} = 4\pi R_\gamma^2 \Delta'_s$, where $\Delta'_s = R_\gamma/2\Gamma$ is the comoving thickness of the emitting shell and R_γ is the distance from the central engine where the electromagnetic radiation is produced. Dissipation—whether it occurs in the photosphere, in the optically thin region (e.g., ISs) or external shocks—causes the conversion of a fraction ε_d of the total jet energy \tilde{E}_{iso} into thermal energy, bulk kinetic energy, non-thermal particle energy, and magnetic energy. The energy stored in relativistic

Table 1. Characteristic parameters assumed for our benchmark GRB jet for the scenarios considered in this paper: internal shock (IS) model, dissipative photosphere model with internal shocks (PH-IS), three components model (3-COMP), ICMART model, magnetized jet model with gradual dissipation (MAG-DISS), and proton synchrotron model (p-SYNCH). In the case of quantities varying along the jet, the variability range is reported. The dissipation efficiency ε_{IS} has been taken from Ref. [69]. For the magnetic model with gradual dissipation, the electron fraction, the electron power-law index, and the proton power-law index are defined in Eqs. 2.13, and 2.15, respectively.

Parameter	Symbol	Model					
		IS	PH-IS	3-COMP	ICMART	MAG-DISS	p-SYNCH
Total jet energy	\tilde{E}_{iso}	3.4×10^{54} erg					n/a
Jet opening angle	θ_j	3°					
Lorentz boost factor	Γ	300					
Redshift	z	2					
Duration of the burst	t_{dur}	100 s					
Variability time scale	t_v	0.5 s					
Dissipation efficiency	ε_d	$\varepsilon_{\text{IS}} = 0.2$	$\varepsilon_{\text{IS}} = 0.03$	n/a	$\varepsilon_d = 0.35$	0.24	n/a
Electron energy fraction	ε_e	1/12			0.5	0.35 – 0.36	n/a
Proton energy fraction	ε_p	10/12			0.5	0.64 – 0.65	n/a
Electron power-law index	k_e	n/a	2.5	n/a		2.4 – 2.6	n/a
Proton power-law index	k_p	2				2.4 – 2.6	2.6
Magnetization at R_γ	σ	n/a			45	1.35 – 1.81	n/a

electrons, protons, and magnetic fields in the emitting region can be parameterized through the fractions ε_p , ε_e and ε_B , respectively.

These parameters ignore the detailed microphysics at the plasma level, but allow to establish a direct connection with the observables. We assume that energy equipartition between electrons and magnetic fields occurs at the ISs, and 10 times more energy goes into protons, namely: $\varepsilon_e = \varepsilon_B = 1/12$ and $\varepsilon_p/\varepsilon_e = 10$. For the magnetized jet models, instead, these parameters may depend on the magnetization of the jet, as we will see later. At the external shock, in the deceleration phase, we adopt $\varepsilon_e = 4 \times 10^{-2}$, $\varepsilon_B = 10^{-4}$ and $\varepsilon_p = 1 - \varepsilon_e - \varepsilon_B$ [106–108]

For what concerns the energetics of our reference jet, motivated by recent observations of GRB afterglows [109], we choose $\tilde{E}_{\text{iso}} = 3.4 \times 10^{54}$ ergs, where a typical opening angle of $\theta_j = 3$ degrees is adopted. Our benchmark Lorentz factor is $\Gamma = \Gamma_{\text{sat}} = 300$ [110]. The duration of the burst is taken to be $\tilde{t}_{\text{dur}} = 100 \text{ s}/(1 + z)$, where $z = 2$ is the redshift we adopt for our reference GRB. Finally we use $t_v = 0.5$ s as the variability timescale of the GRB lightcurve [31]. The parameters adopted for each model for our benchmark GRB are summarized in Table 1.

A quantity that allows to compare among different models is the radiative efficiency of the jet, defined as the fraction of the total jet energy which is radiated in photons [111]:

$$\eta_\gamma = \frac{\tilde{E}_{\gamma,\text{iso}}}{\tilde{E}_{\text{iso}}} . \quad (3.1)$$

For example $\eta_\gamma = \varepsilon_{\text{PH}}$ when the dominant radiation is of photospheric origin or $\eta_\gamma = \varepsilon_{\text{IS}}\varepsilon_e$ when the radiation is produced at the IS, assuming a fast cooling regime for electrons.

3.2 Spectral energy distribution of protons

For the purposes of this work, it is sufficient to assume that protons and electrons in the dissipation site are accelerated via Fermi-like mechanisms³. The accelerated particles acquire a non-thermal energy distribution that can be phenomenologically described as [115]:

$$n'_p(E'_p) = AE'_p{}^{-k} \exp \left[- \left(\frac{E'_p}{E'_{p,\max}} \right)^{\alpha_p} \right] \Theta(E'_p - E'_{p,\min}) , \quad (3.2)$$

where $A = U'_p \left[\int_{E'_{p,\min}}^{E'_{p,\max}} n'_p(E'_p) E'_p dE'_p \right]^{-1}$ is the normalization of the spectrum (in units of $\text{GeV}^{-1} \text{cm}^{-3}$) and Θ is the Heaviside function, with $U'_p = \varepsilon_p \varepsilon_d E'_{\text{iso}}$ being the fraction of the dissipated jet energy that goes into acceleration of protons. The power-law index is found to be $k \approx 2.3$ in the ultra-relativistic shock limit in semi-analytical and Monte Carlo simulations, although it is predicted to be steeper from particle-in-cell simulations [116]. The power-law index is instead $k = 2$ for a non-relativistic shock [117], while it depends on the jet magnetization for magnetically dominated jets, as we will see later. The exponential cut-off with α_p is due to energy losses of protons and we adopt $\alpha_p = 2$ following Ref. [118], $E'_{p,\min}$ is the minimum energy of the protons that are injected within the acceleration region, and $E'_{p,\max}$ is the maximum proton energy. The latter is constrained by the Larmor radius being smaller than the size of the acceleration region, or imposing that the acceleration timescale,

$$t'_{p,\text{acc}}{}^{-1} = \frac{\zeta c e B'}{E'_p} , \quad (3.3)$$

is shorter than the total cooling timescale for protons. Here $\zeta = 1$ is the acceleration efficiency adopted throughout this work. The total cooling timescale is given by

$$t'_{p,\text{cool}}{}^{-1} = t'_{\text{sync}}{}^{-1} + t'_{p,\text{IC}}{}^{-1} + t'_{p,\text{BH}}{}^{-1} + t'_{p\gamma}{}^{-1} + t'_{p,\text{hc}}{}^{-1} + t'_{p,\text{ad}}{}^{-1} ; \quad (3.4)$$

where t'_{sync} , $t'_{p,\text{IC}}$, $t'_{p,\text{BH}}$, $t'_{p\gamma}$, $t'_{p,\text{hc}}$, $t'_{p,\text{ad}}$ are the proton synchrotron (sync), inverse Compton (IC), Bethe-Heitler ($p\gamma \rightarrow pe^+e^-$, BH), hadronic (hc) and adiabatic (ad) cooling times, respectively. They are defined as follows [59, 119, 120]:

$$t'_{p,\text{sync}}{}^{-1} = \frac{4\sigma_T m_e^2 E'_p B'^2}{3m_p^4 c^3 8\pi} , \quad (3.5)$$

$$t'_{p,\text{IC}}{}^{-1} = \frac{3(m_e c^2)^2 \sigma_T c}{16\gamma_p'^2 (\gamma_p' - 1) \beta_p'} \int_{E'_{\gamma,\min}}^{E'_{\gamma,\max}} \frac{dE'_\gamma}{E_\gamma'^2} F(E'_\gamma, \gamma_p') n'_\gamma(E'_\gamma) , \quad (3.6)$$

$$t'_{p,\text{BH}}{}^{-1} = \frac{7m_e \alpha \sigma_T c}{9\sqrt{2}\pi m_p \gamma_p'^2} \int_{\gamma_p'^{-1}}^{\frac{E'_{\gamma,\max}}{m_e c^2}} d\epsilon' \frac{n'_\gamma(\epsilon')}{\epsilon'^2} \left\{ (2\gamma_p' \epsilon')^{3/2} \left[\ln(\gamma_p' \epsilon') - \frac{2}{3} \right] + \frac{2^{5/2}}{3} \right\} , \quad (3.7)$$

$$t'_{p\gamma}{}^{-1} = \frac{c}{2\gamma_p'^2} \int_{\frac{E_{\text{th}}}{2\gamma_p'}}^{\infty} d\epsilon'_\gamma \frac{n'_\gamma(E'_\gamma)}{E_\gamma'^2} \int_{E_{\text{th}}}^{2\gamma_p' E'_\gamma} dE_r E_r \sigma_{p\gamma}(E_r) K_{p\gamma}(E_r) , \quad (3.8)$$

$$t'_{\text{hc}}{}^{-1} = c n'_p \sigma_{pp} K_{pp} , \quad (3.9)$$

$$t'_{p,\text{ad}}{}^{-1} = \frac{2c\Gamma}{R} . \quad (3.10)$$

³In the reconnection region there are various particle acceleration sites, see e.g. Ref. [112]. It remains a matter of active research what is the dominant process responsible for the formation of the power-law, see e.g. Refs. [100, 101, 112–114]

In the definitions above, $\epsilon' = E'_\gamma/m_e c^2$, $\gamma'_p = E'_p/m_p c^2$, and $\alpha = 1/137$ is the fine structure constant. The cross sections $\sigma_{p\gamma}$ and σ_{pp} , for $p\gamma$ and pp interactions respectively, are taken from Ref. [121]. The function $F(E'_\gamma, \gamma'_p)$ is provided in Ref. [122], while $K_{p\gamma}$ is the inelasticity of $p\gamma$ collisions [59]:

$$K_{p\gamma}(E_r) = \begin{cases} 0.2 & E_{\text{th}} < E_r < 1 \text{ GeV} \\ 0.6 & E_r > 1 \text{ GeV} \end{cases}, \quad (3.11)$$

where $E_r = \gamma'_p E'_\gamma (1 - \beta'_p \cos \theta')$ is the relative energy between a proton with gamma factor γ'_p and a photon of energy E'_γ , whose directions form an angle θ' in the comoving system, $E_{\text{th}} = 0.15 \text{ GeV}$ is the threshold for the photo-hadronic interaction, $n'_\gamma(E'_\gamma)$ is the target photon density field (in units of $\text{GeV}^{-1} \text{cm}^{-3}$), $K_{pp} = 0.8$, and n'_p is the comoving proton density defined as $n'_p = n'_b/2$, where n'_b is the baryonic density defined in Eq. 2.1. As we will see in Sec. 5.3, the proton synchrotron scenario is such that the properties of the proton distribution (e.g., minimum energy, power-law slope), as well as the shape of energy distribution itself, can be directly inferred from the observed GRB prompt spectra.

4 Neutrino production in the gamma-ray burst jet

The simultaneous presence of a high density target photon field in the site of proton acceleration—that can be radiated by co-accelerated electrons, by protons themselves or have an external origin—leads to an efficient production of high-energy neutrinos through photo-hadronic interactions. Since the number of target photons is always much larger than the number density of non-relativistic (cold) protons in all cases of study, we neglect the pp contribution.

Photo-hadronic interactions lead to charged pion and kaon (as well as neutron) production, which subsequently cool and decay in muons and neutrinos. According to the standard picture, pion production occurs through the $\Delta(1232)$ resonance channel:

$$p + \gamma \longrightarrow \Delta^+ \longrightarrow \begin{cases} n + \pi^+ & 1/3 \text{ of all cases} \\ p + \pi^0 & 2/3 \text{ of all cases} \end{cases} \quad (4.1)$$

followed by the decay chain

$$\pi^+ \rightarrow \mu^+ + \nu_\mu \quad (4.2)$$

$$\mu^+ \rightarrow \bar{\nu}_\mu + \nu_e + e^+ . \quad (4.3)$$

In order to accurately estimate the neutrino spectral energy distribution and the related neutrino flavor ratio, we rely on the photo-hadronic interaction model of Ref. [118] (model Sim-B and Sim-C) based on SOPHIA [123]. The latter includes higher resonances, direct and multi-pion production contributions. Note that, although we compute the neutrino and antineutrino spectral distributions separately, in the following we do not distinguish between them unless otherwise specified.

Given the photon and proton energy distributions in the comoving frame, $n'_\gamma(E'_\gamma)$ and $n'_p(E'_p)$, the production rate of secondary particles is given by (in units of $\text{GeV}^{-1} \text{cm}^{-3} \text{s}^{-1}$)

$$Q'_l(E'_l) = \int_{E'_l}^{\infty} \frac{dE'_p}{E'_p} n'_p(E'_p) \int_{E_{\text{th}}/2\gamma'_p}^{\infty} dE'_\gamma n'_\gamma(E'_\gamma) R_\alpha(x, y) , \quad (4.4)$$

where $x = E'_l/E'_p$ is the fraction of proton energy going into daughter particles, $y = \gamma'_p E'_\gamma$, and l stands for π^+ , π^- , π^0 , and K^+ . Since kaons suffer less from radiative cooling than charged

pions due to their larger mass and shorter lifetime, their contribution to the neutrino flux becomes important at high energies [36, 124, 125], whilst it is sub-leading at lower energies, given the low branching ratio for their production. The “response function” $R_l(x, y)$ contains all the information about the interaction type (cross section and multiplicity of the products); we refer the interested reader to Ref. [118] for more details.

Once produced, the charged mesons undergo different energy losses before decaying into neutrinos. Their energy distribution at decay is

$$Q_l^{\text{dec}}(E_l') = Q_l'(E_l') \left[1 - \exp\left(-\frac{t_{l,\text{cool}}'}{E_l' \tau_l'}\right) \right], \quad (4.5)$$

with $t_{l,\text{cool}}'$ being the cooling time scale and τ_l' the lifetime of the meson l . The neutrino energy distribution originating from the decay processes like the one in Eq. 4.2 is

$$Q'_{\nu_\alpha}(E'_{\nu_\alpha}) = \int_{E'_{\nu_\alpha}}^{\infty} Q_l^{\text{dec}}(E_l') \frac{1}{E_l'} F_{l \rightarrow \nu_\alpha} \left(\frac{E'_{\nu_\alpha}}{E_l'} \right), \quad (4.6)$$

where $F_{l \rightarrow \nu_\alpha}$ is defined in Ref. [115] for ultra-relativistic parent particles. The same procedure is followed for antineutrinos.

The steps above also allow to compute the spectra of charged muons, with an additional dependence on the muon helicity. Again, the cooled muon spectra are derived as in Eq. 4.5 and the neutrinos generated by the muon decay are computed following Ref. [115].

The total neutrino injection rate $Q'_{\nu_\alpha}(E'_{\nu_\alpha})$ at the source is obtained by summing over the contributions from all channels. Finally, the fluence for the flavor ν_α at Earth from a source at redshift z is (in units of $\text{GeV}^{-1} \text{cm}^{-2}$)

$$\Phi_{\nu_\alpha}(E_{\nu_\alpha}, z) = \hat{N} \frac{(1+z)^2}{4\pi d_L^2(z)} \sum_{\beta} P_{\nu_\beta \rightarrow \nu_\alpha}(E_{\nu_\alpha}) Q'_{\nu_\beta} \left[\frac{E_{\nu_\alpha}(1+z)}{\Gamma} \right], \quad (4.7)$$

where [29]

$$P_{\nu_e \rightarrow \nu_\mu} = P_{\nu_\mu \rightarrow \nu_e} = P_{\nu_e \rightarrow \nu_\tau} = \frac{1}{4} \sin^2 2\theta_{12}, \quad (4.8)$$

$$P_{\nu_\mu \rightarrow \nu_\mu} = P_{\nu_\mu \rightarrow \nu_\tau} = \frac{1}{8} (4 - \sin^2 2\theta_{12}), \quad (4.9)$$

$$P_{\nu_e \rightarrow \nu_e} = 1 - \frac{1}{2} \sin^2 2\theta_{12}, \quad (4.10)$$

with $\theta_{12} \simeq 33.5$ degrees [126], $P_{\nu_\beta \rightarrow \nu_\alpha} = P_{\bar{\nu}_\beta \rightarrow \bar{\nu}_\alpha}$, and $\hat{N} = V'_{\text{iso},s} t_{\text{dur}}$ [127] being the normalization factor depending on the volume of the interaction region. The luminosity distance $d_L(z)$ is defined in a flat Λ CDM cosmology as

$$d_L(z) = (1+z) \frac{c}{H_0} \int_0^z \frac{dz'}{\sqrt{\Omega_\Lambda + \Omega_M(1+z')^3}} \quad (4.11)$$

with $\Omega_M = 0.315$, $\Omega_\Lambda = 0.685$ and the Hubble constant $H_0 = 67.4 \text{ km s}^{-1} \text{ Mpc}^{-1}$ [128].

5 Results: Gamma-ray burst neutrino emission

Each of the dissipation mechanisms introduced in Sec. 2, according to the radius at which it takes place, leads to different photon energy distributions. In Appendix A we report the empirical functions usually adopted to fit the observed photon spectra. For each of the GRB models considered in this section, we assume that the spectral energy distribution of photons is either given by one of the fitting functions or a combination of them. In this section, we investigate the neutrino production in the prompt phase for each scenario.

5.1 Kinetic dominated jets

5.1.1 Jet model with internal shocks

We focus on the IS model introduced in Sec. 2.1.1 with the photon spectrum produced at the IS radius and described by the Band function in Eq. A.2. The radiative efficiency is $\eta_\gamma = \varepsilon_{\text{IS}}\varepsilon_e \simeq 0.02$ (see Table 1).

In order to establish the relative importance of the various energy loss processes in this scenario, we compute the proton and the secondary particle (K^\pm , π^\pm and μ^\pm) cooling times as illustrated in Sec. 3.2. The cooling times are shown in Fig. 4 as functions of the particle energy in the comoving frame. With the parameters adopted for our benchmark GRB, protons are mainly cooled by adiabatic expansion up to $E'_{p,\text{max}}$ (left panel of Fig. 4), with the second dominant energy loss mechanism being photo-hadronic interactions. For mesons and muons (right panel of Fig. 4) adiabatic and synchrotron cooling at low and high energies, respectively, are the two dominant cooling processes.

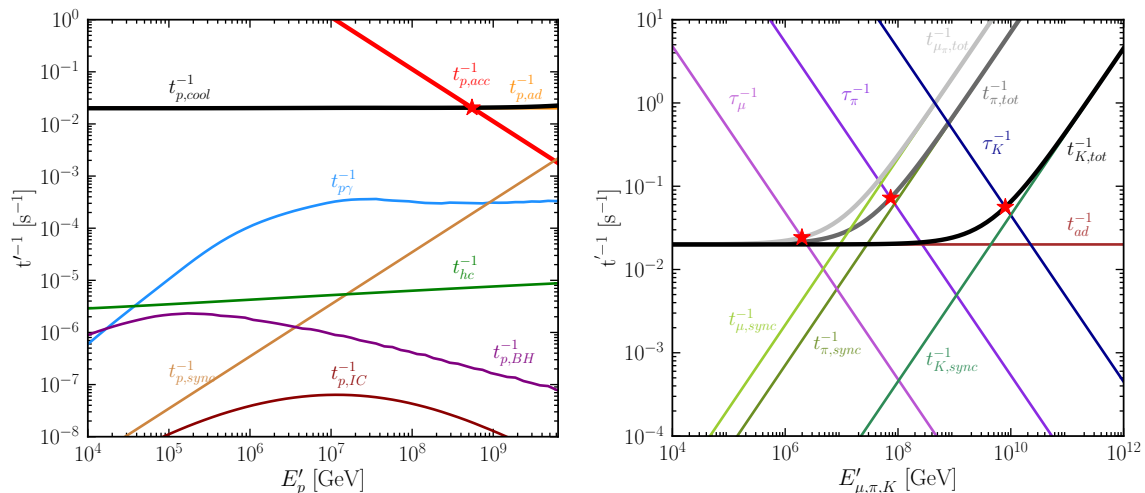


Figure 4. *Left:* Inverse cooling timescales for protons at the IS radius as functions of the proton energy in the comoving frame for our benchmark GRB, see Table 1. The thin solid lines mark the individual cooling processes introduced in Sec. 3.2; the thick black and red solid lines represent the total cooling timescale and the acceleration timescale, respectively. The red star marks the maximum comoving proton energy such that $t'_{p,cool}{}^{-1} = t'_{p,acc}{}^{-1}$. Protons are mainly cooled by adiabatic expansion and $p\gamma$ interactions. *Right:* Analogous to the left panel, but for the inverse cooling timescales for pions, muons, and kaons. The dominant energy losses in this case are adiabatic cooling at low energies and synchrotron cooling at higher energies.

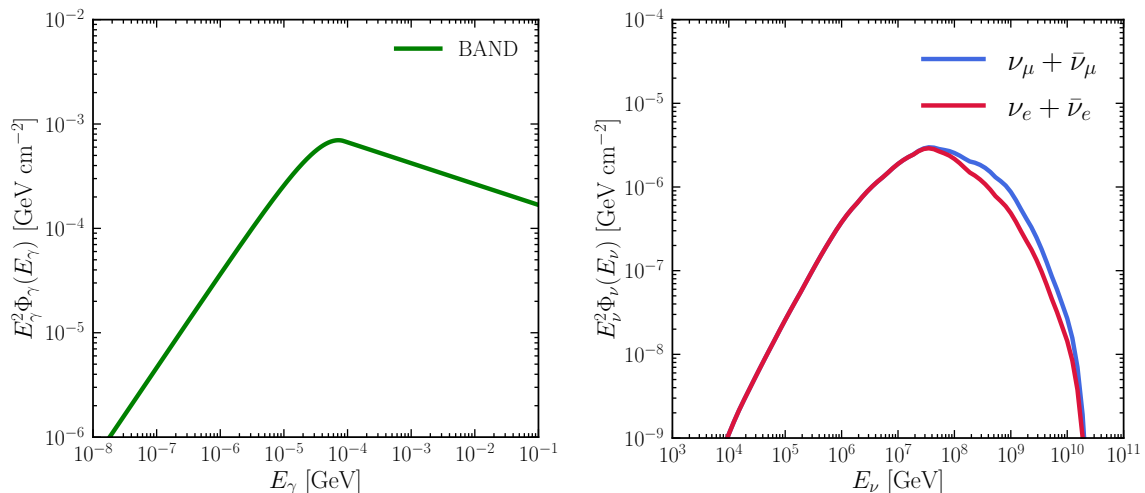


Figure 5. *Left:* Band photon fluence observed at Earth for our benchmark GRB in the IS model, see Table 1. *Right:* Correspondent $\nu_\alpha + \bar{\nu}_\alpha$ fluence in the observer frame (in red for the electron flavor and in blue for the muon flavor) in the presence of flavor conversions. The fluence for the muon flavor peaks at $E_\nu^{\text{peak}} = 3.6 \times 10^7$ GeV.

Following Sec. 4, we compute the neutrino production rate in the comoving frame at R_{IS} and the correspondent fluence at Earth including flavor conversions. The results are shown in the right panel of Fig. 5, while the photon spectrum described by the Band function is shown in the left panel.

Our results are in good agreement with analogous estimations reported in the literature for comparable input parameters, see e.g. Ref. [129]. In this scenario, the fluence for the muon flavor peaks at $E_\nu^{\text{peak}} = 3.6 \times 10^7$ GeV and rapidly declines at higher energies. The effects due to the cooling of kaons are not visible because, as shown in Fig. 4, the maximum proton energy is more than one order of magnitude lower than the one at which kaons cool by synchrotron radiation.

5.1.2 Jet model with a dissipative photosphere and internal shocks

We now explore the model introduced in Sec. 2.1.2 and consider a jet with an efficient photospheric emission, described by a Band spectrum peaking at the energy given by Eq. A.4, and undergoing further IS dissipation. At R_{IS} , protons and electrons are efficiently accelerated and turbulent magnetic fields may build up. In this scenario, electrons cool, other than by emitting synchrotron radiation, also by Compton up-scattering of the non-thermal photospheric photons. As we are interested in investigating the case where the photospheric emission is dominant in the MeV energy range, we consider Case (I) of Table 1 of Ref. [45], corresponding to the luminosity hierarchy $L_{\text{PH}} \gg L_{\text{UP}} \gg L_{\text{SYNC}}$, where L_{PH} , L_{UP} , and L_{SYNC} stand for the photospheric luminosity, up-scattered photospheric luminosity of the accelerated electrons at R_{IS} , and synchrotron luminosity radiated by the electrons at R_{IS} , respectively.

Following Ref. [45], we define

$$x = \frac{\varepsilon_{\text{IS}} \varepsilon_B}{\varepsilon_{\text{PH}}} \quad \text{and} \quad Y = \frac{U'_{\text{SYNC}}}{U'_B} = \frac{4}{3} \frac{(k_e - 1)}{(k_e - 2)} \tau_T \gamma'_{e,\text{min}} \gamma'_{e,\text{cool}} h, \quad (5.1)$$

where Y is the Compton parameter, k_e is the slope of the electron energy distribution, h is a function of $\gamma'_{e,\min}$ and $\gamma'_{e,\text{cool}}$ and depends on the cooling regime, $\gamma'_{e,\min}$ is the minimum Lorentz factor of the electrons injected in the acceleration region

$$\gamma'_{e,\min} = \frac{m_p k_e - 2}{m_e k_e - 1} \mathcal{R}^{-1} \xi^{-1} \varepsilon_{\text{IS}} \varepsilon_e, \quad (5.2)$$

with ξ being the fraction of electrons accelerated at the shock and \mathcal{R} being the number of leptons per baryon. Finally, $\gamma'_{e,\text{cool}}$ is the electron cooling Lorentz factor obtained from $\gamma'_{e,\text{cool}} m_e c^2 = P(\gamma'_{e,\text{cool}}) t'_{\text{ad}}$ and given by

$$\gamma'_{e,\text{cool}}(R) \simeq \frac{3m_e \mathcal{R}}{4m_p \tau_T \varepsilon_{\text{PH}}} \frac{1}{x(1+Y) + 1}; \quad (5.3)$$

t'_{ad} being the adiabatic cooling timescale and $P(\gamma'_{e,\text{cool}}) = 4/3 \sigma_{\text{T}} c \gamma'_{e,\text{cool}}{}^2 (U'_{\text{B}} + U'_{\text{SYNC}} + U'_{\text{PH}})$ the cooling rate for electrons. The conditions we need to fulfill in order to satisfy $L_{\text{PH}} \gg L_{\text{UP}} \gg L_{\text{SYNC}}$ are

$$\eta < \eta_*, \quad x \ll 1, \quad xY \ll 1, \quad Y = \frac{\varepsilon_{\text{IS}} \varepsilon_e h}{\varepsilon_{\text{PH}}} \ll 1. \quad (5.4)$$

In this way, it is possible to estimate $L_{\text{UP}} = Y L_{\text{PH}}$ and $L_{\text{SYNC}} = xY L_{\text{PH}}$.

We adopt the electron slope $k_e = 2.5$ and fix ε_{IS} by relying on the observations in the optical band; by assuming that the synchrotron extended emission in this range should not be brighter than what is typically observed, the following constraint on the flux holds: $F_{\nu}^{\text{sync}}(E_{\gamma,\text{opt}}) < 100$ mJy with $E_{\gamma,\text{opt}} = 2$ eV [130]. In our case, $\varepsilon_{\text{IS}} \leq 0.03$ satisfies such a condition. The radiative efficiency of this GRB is $\eta_{\gamma} = (\tilde{E}_{\text{PH}} + \tilde{E}_{\text{SYNC}} + \tilde{E}_{\text{UP}}) / \tilde{E}_{\text{iso}} = \tilde{E}_{\text{PH}}(1 + Y + xY) / \tilde{E}_{\text{iso}} \simeq 0.2$. Since the high-energy photospheric photons are absorbed by the e^{\pm} pair creation at R_{PH} , we use a cut-off for the Band spectrum at R_{PH} , defined in Eq. A.1.

We define the total photon energy distribution in the comoving frame at R_{IS} as

$$n'_{\gamma,\text{tot}}(E'_{\gamma}) = \left(\frac{R_{\text{PH}}}{R_{\text{IS}}} \right)^2 n'_{\gamma,\text{PH}}(E'_{\gamma}) + n'_{\gamma,\text{SYNC}}(E'_{\gamma}) + n'_{\gamma,\text{UP}}(E'_{\gamma}) \quad (5.5)$$

and compute the cooling processes of protons at the IS. The results are qualitatively similar to those shown in Fig. 4, except for the BH cooling being strongly dominant over the pp one, and $t_{p\gamma}$ being much shorter [$\mathcal{O}(40)$] than in the IS case; this is due to the larger photon number density at R_{IS} . Synchrotron losses are negligible. Furthermore, the acceleration timescale in this scenario is much longer due to a weaker magnetic field in the acceleration region. This sets the proton energy distribution cutoff at a lower energy than before ($E'_{p,\text{max}} \sim 1.2 \times 10^8$ GeV).

Figure 6 shows the resultant photon (on the left panel) and neutrino (on the right panel) fluences for the IS shock scenario with a dissipative photosphere. The black curve in the left panel represents the overall photon fluence. The total spectrum is consistent with Fermi observations [131], being the high energy component subdominant with respect to the Band one. From the right panel, one can see that the muon fluence peaks at $E_{\nu}^{\text{peak}} = 6.4 \times 10^7$ GeV and it is comparable in normalization to the one of the IS model (see Fig. 5). This is due to a counterbalance between the radiative inefficiency in the IS model and a lower high energy proton number density in this scenario. Similar conclusions are reported in Ref. [132], where a further reduction in the neutrino production efficiency is envisaged as due to the anisotropy

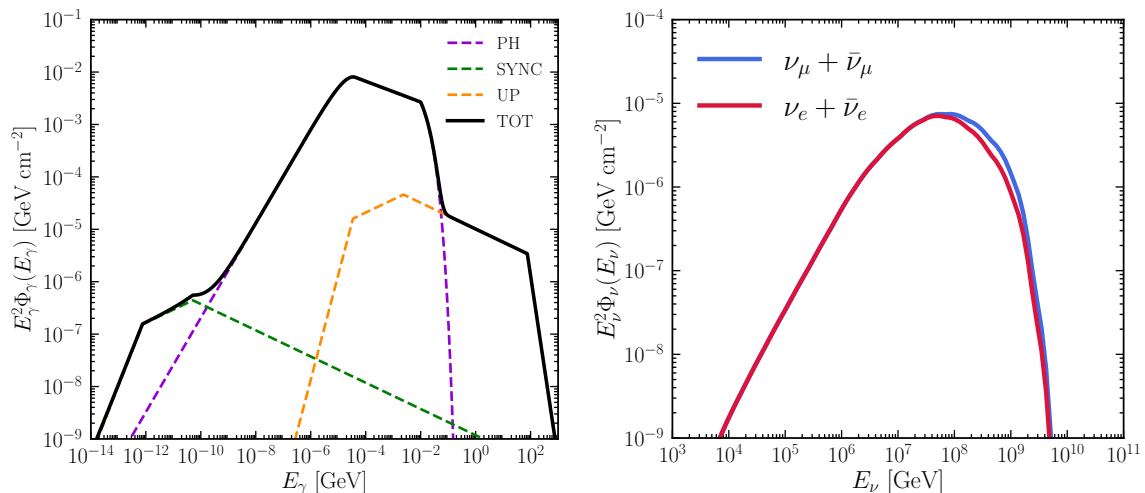


Figure 6. *Left:* Photon fluence observed at Earth for the IS model with dissipative photosphere. The photospheric emission (PH, violet line), the photospheric up-scattered emission (UP, orange line), and the synchrotron emission of electrons accelerated at R_{IS} (SYNC, green line) are plotted together with the total photon fluence (in black). *Right:* $\nu_\alpha + \bar{\nu}_\alpha$ fluence in the observer frame produced at R_{IS} with flavor oscillations included (in red for electron and blue for muon flavors). The astrophysical parameters for this GRB are reported in Table 1, and $\bar{E}_{\text{PH}} = 6.8 \times 10^{53}$ erg, $\bar{E}_{\text{SYNC}} \simeq 4.7 \times 10^{49}$ erg, $\bar{E}_{\text{UP}} \simeq 4.7 \times 10^{51}$ erg, $\mathcal{R} = 20$, $\xi = 1$. The fluence for the muon flavor peaks at $E_{\nu}^{\text{peak}} = 6.4 \times 10^7$ GeV and its normalization is comparable to the one in Fig. 5. This is due to a counterbalance between the radiative inefficiency in the IS model and the lower high energy proton density in this scenario.

of the incoming photon field at R_{IS} , an effect that we do not take into account here. Finally, the high energy tail of the distribution has a decline sharper in this scenario than in the IS case because of the lower proton energy cutoff. The low $E'_{p,\text{max}}$ is also the reason why spectral modifications due to kaon decay are not visible ($E'_{\pi,\text{max}}, E'_{K,\text{max}} > E'_{p,\text{max}}$).

5.1.3 Jet model with three emission components

We are interested in a representative GRB of the class of bursts introduced in Sec. 2.1.3, hence we adopt average values for the spectral index and intensity of each component. To this purpose, we rely on Refs. [46, 133, 134].

Once the outflow becomes transparent to radiation, a BB component is emitted at R_{PH} , with spectral index $\alpha_{\text{BB}} = 0.4$ [41] and peaks at the temperature defined in Eq. 2.4. Subsequently, the kinetic energy of the outflow is dissipated at the ISs, and the main spectral component (CPL1) is produced. The latter is described by a CPL with spectral index $\alpha_{\text{CPL1}} = -1$. An additional cut-off power-law (CPL2) begins to appear after a slight delay with respect to CPL1, with the cut-off shifting to higher energies until its disappearance. At later times, this additional component is well described by a simple PL, and we associate it to the beginning of the afterglow. With this choice, we take into account both interpretations of the additional energetic component, namely the internal or external origin of CPL2.

At the deceleration radius R_{dec} (see Eq. 2.7), the external shock starts accelerating protons and electrons of the wind and the magnetic field builds up. Motivated by the afterglow modeling [135], we use the following values for the energy fractions: $\varepsilon_e = 4 \times 10^{-2}$, $\varepsilon_B = 10^{-4}$ and $\varepsilon_p = 1 - \varepsilon_e - \varepsilon_B$ [108], compatible with our choice for the prompt efficiency.

We consider a wind type circumburst medium with $A = 3 \times 10^{34} \text{ cm}^{-1}$ [136] and an adiabatic blastwave, with $\Gamma(t) = \Gamma(t_{\text{dec}}/4t)^{1/4}$ [136] and $R(t) = 2\Gamma^2(t)ct/(1+z)$ describing the temporal evolution of the Lorentz factor and the radius of the forward shock after t_{dec} , respectively. The energy of the accelerated particles in the blastwave, at a time t after the deceleration, is $\tilde{U}_p = 4\pi\varepsilon_p AR(t)m_p c^2[\Gamma^2(t) - 1]$. By relying on the temporal evolution of the bright GRB investigated in Ref. [137], we consider a simple PL produced at the forward shock, with power slope $\alpha_{\text{PL}} = -1.8$ (Eq. A.6), and normalize it to $\tilde{E}_{\text{PL}} = \varepsilon_e/\varepsilon_p \tilde{U}_p$. The photon field target for $p\gamma$ interactions at the forward shock is the sum of the PL, BB and CPL1 components; the latter two being Lorentz transformed in the comoving frame of the blastwave.

Since we are interested in computing the neutrino fluence emitted at the forward shock during the prompt phase, we take a representative average radius R_* in logarithmic scale between R_{dec} and $R(t_{\text{dur}} - t_{\text{dec}})$. The photon energy distribution is

$$n'_{\text{tot}}(E'_\gamma, R_*) = n'_{\text{PL}}(E'_\gamma) + \left(\frac{R_{\text{PH}}}{R_*}\right)^2 n'_{\text{BB}}\left(\frac{E'_\gamma}{\Gamma_r}\right) + \left(\frac{R_{\text{IS}}}{R_*}\right)^2 n'_{\text{CPL1}}\left(\frac{E'_\gamma}{\Gamma_r}\right), \quad (5.6)$$

where Γ_r is the relative Lorentz factor between Γ and $\Gamma_* \equiv \Gamma(R_*)$.

The BB component is always subdominant, while CPL1 and CPL2 are expected to vary in absolute and relative intensity from burst to burst; this is true also in the same GRB, once the temporal evolution is considered. In order to investigate to what extent the neutrino spectrum may be affected by these factors, we considered two scenarios of study for the prompt phase: case (I) such that the energetics of the three components is $\tilde{E}_{\text{BB}} \simeq 0.1\tilde{E}_{\text{CPL1}}$ and $\tilde{E}_{\text{CPL1}} = 3\tilde{E}_{\text{CPL2}}$ (solid black line in the top left panel of Fig. 7) and case (II) with $\tilde{E}_{\text{CPL1}} = 1/3\tilde{E}_{\text{CPL2}}$ (dotted black line in the top left panel of Fig. 7). The three cut-off power-laws (BB, CPL1, and CPL2) follow Eq. A.5 with peak energies $E_{\text{BB,peak}} \simeq 2 \times 10^{-5} \text{ GeV}$, $E_{\text{CPL1,peak}} \simeq 7 \times 10^{-5} \text{ GeV}$, and $E_{\text{CPL2,peak}} \simeq 2 \times 10^{-2} \text{ GeV}$, respectively. These values are consistent with the ones in Refs. [46, 137]. With this set of parameters, the hierarchy and intensity of the various cooling processes is analogous to the IS case for the prompt phase (Fig. 4), while adiabatic cooling is the dominant cooling process by many orders of magnitude at R_* . For what concerns the forward shock, we assume a differential number density of protons $n'_p(E'_p) \propto E'_p{}^{-2}$ injected between the minimum energy $E'_{p,\text{min}} = m_p c^2 \Gamma_*$ and the maximum $E'_{p,\text{max}}$, derived from the condition that the proton acceleration time t'_{acc} is limited by the adiabatic time t'_{ad} (see Sec. 3.2).

The neutrino fluence at the IS and forward shock is displayed in Fig. 7. In the top left panel, the solid line represents the neutrino fluence for case (I), while the dotted line stands for case (II). The enhancement of the energetic component CPL2 of almost one order of magnitude leads to a negligible impact on the neutrino energy distribution, producing only a slight increase of the fluence at low energies.

The bottom panels of Fig. 7 display the photon fluence and the correspondent neutrino fluence when the emission from the forward shock starts during the prompt phase. The dashed lines represent the neutrino fluence produced at the IS from the interaction of accelerated protons and the photon field (BB+CPL1), while the dash-dotted line represents the neutrino outcome from the forward shock at R_* , where we rely on Eq. 5.6 for the photon field. The solid line describes the total neutrino fluence expected during the prompt phase. The forward shock contribution is significantly higher than what expected for the afterglow phase [136]. This is mainly due to a much larger photon number density in the acceleration region. Furthermore, given the very low magnetic field and its inefficiency to

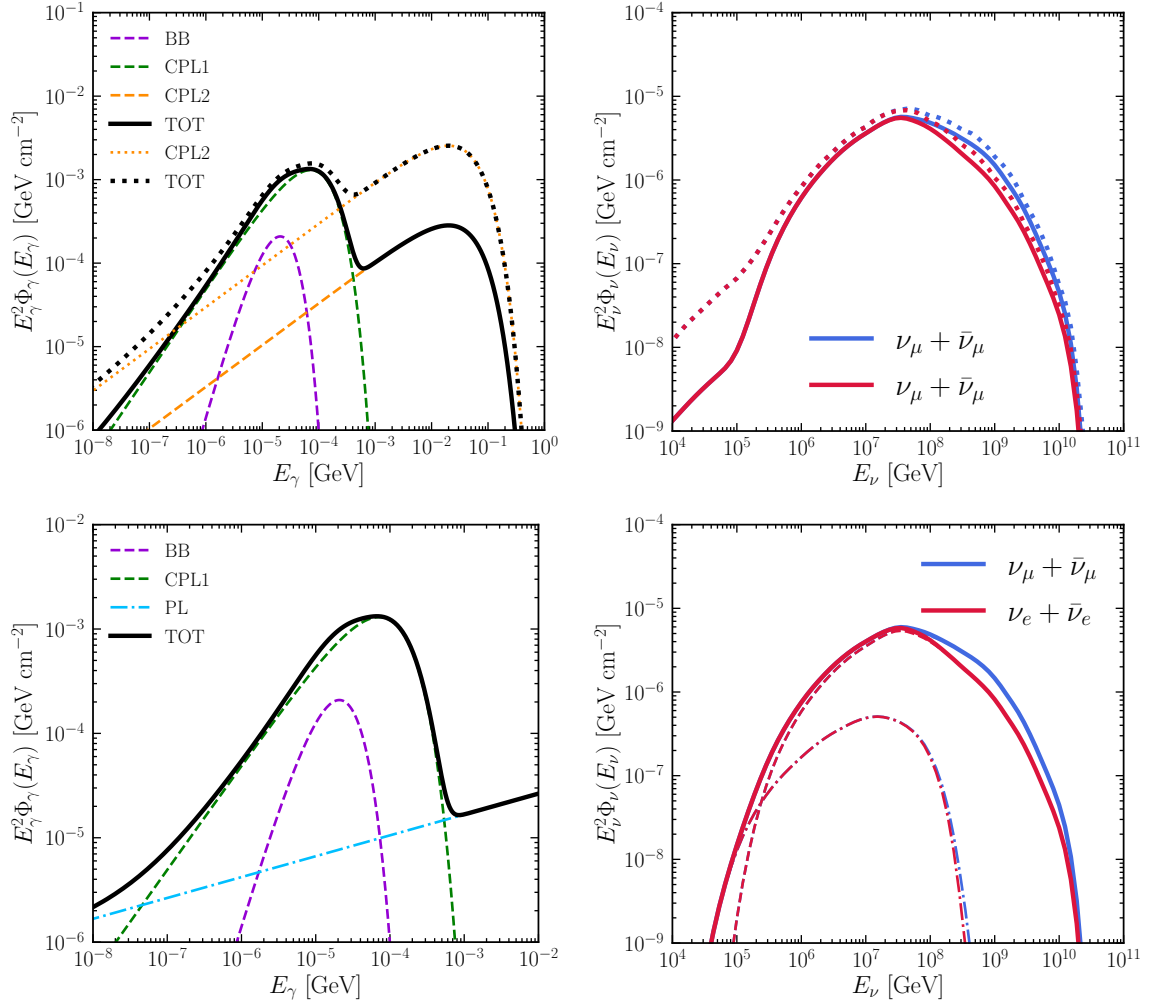


Figure 7. *Top left:* Photon fluence in the prompt phase for the model with three components. It is composed by a thermal BB component (violet dashed curve), a cut-off power law CPL1 (green dashed curve), and a second cut-off power law CPL2 (in orange dashed for case (I) such $\tilde{E}_{\text{CPL1}} = 3\tilde{E}_{\text{CPL2}}$; in orange dotted for case (II) with $\tilde{E}_{\text{CPL1}} = 1/3\tilde{E}_{\text{CPL2}}$). Furthermore $\tilde{E}_{\text{BB}} = 0.1\tilde{E}_{\text{CPL1}}$. The total fluence is plotted in black (solid and dotted lines). *Top right:* Correspondent $\nu_\alpha + \bar{\nu}_\alpha$ fluence in the observer frame with flavor oscillations included (in red for electron and blue for muon flavors). The solid line represents the total contribution during the prompt for case (I), while the dotted one is for case (II). The fluence for the muon flavor peaks at $E_\nu^{\text{peak}} = 4 \times 10^7$ GeV for the case (I). The low energy tail is affected by the interaction of protons with CPL2. *Bottom left:* Photon fluence for the scenario such that the emission from the forward shock (PL, blue dash-dotted line) starts during the prompt phase (dashed, BB+CPL1). *Bottom right:* Corresponding $\nu_\alpha + \bar{\nu}_\alpha$ fluence (dashed curve for the IS emission, dash-dotted for the forward shock, and solid line for the total).

accelerate particles to very high energies, the cutoff in the neutrino spectrum occurs at a lower energy compared to the prompt case (see dot-dashed line). The overall intensity at peak energy of the neutrino emission in this scenario is comparable to the IS case with a dissipative photosphere.

5.2 Poynting flux dominated jets

5.2.1 ICMART model

For the model introduced in Sec. 2.2.1, the typical radius necessary to make sure that runaway reconnection has enough time to grow is $R_{\text{ICMART}} \simeq 10^{15}$ cm [47], while the typical width of the reconnection region is $\Delta = ct_v$, where we adopt $t_v \simeq 0.5$ s. The dissipation efficiency may be as high as 0.35 in this model [138] and this is the value we adopt for ε_d .

It has been shown that a Band-like spectrum may be reproduced in this scenario by considering an appropriate time dependent injection rate of particles in the emitting region [139], and this is the spectrum we adopt for this model. If σ is the magnetization parameter at R_{ICMART} , the magnetic field in the bulk comoving frame can be expressed as [47]:

$$B' = \left(\frac{2\tilde{L}_{\text{iso}}}{\Gamma^2 c R_{\text{ICMART}}^2} \frac{\sigma}{\sigma + 1} \right)^{1/2}. \quad (5.7)$$

We use as initial jet magnetization $\sigma_0 = \sigma_{\text{in}} = 45$ (see Fig. 2); this choice, as shown in the following, allows for a consistent comparison with the results of Sec. 5.2.2. By relying on the results from particle-in-cell simulations, we assume $k_p(\sigma_0) \simeq 2$ (see Eq. 2.15). Furthermore, we set $\varepsilon_p = 0.5$ and $\varepsilon_e = 0.5$ (see Eq. 2.13). With this choice, the radiative efficiency of our benchmark GRB turns out to be $\eta_\gamma = \varepsilon_d \varepsilon_e \simeq 0.17$. The photon number density is normalized to $\eta_\gamma E'_{\text{iso}}$. Since $R_{\text{IS}} \simeq R_{\text{ICMART}}$, we obtain similar trends for the cooling times as in Fig. 4, except for the synchrotron loss that starts to dominate at $E'_p \sim 10^8$ GeV and a slightly increased rate of $p\gamma$ interactions due to a larger photon number density in the dissipation region.

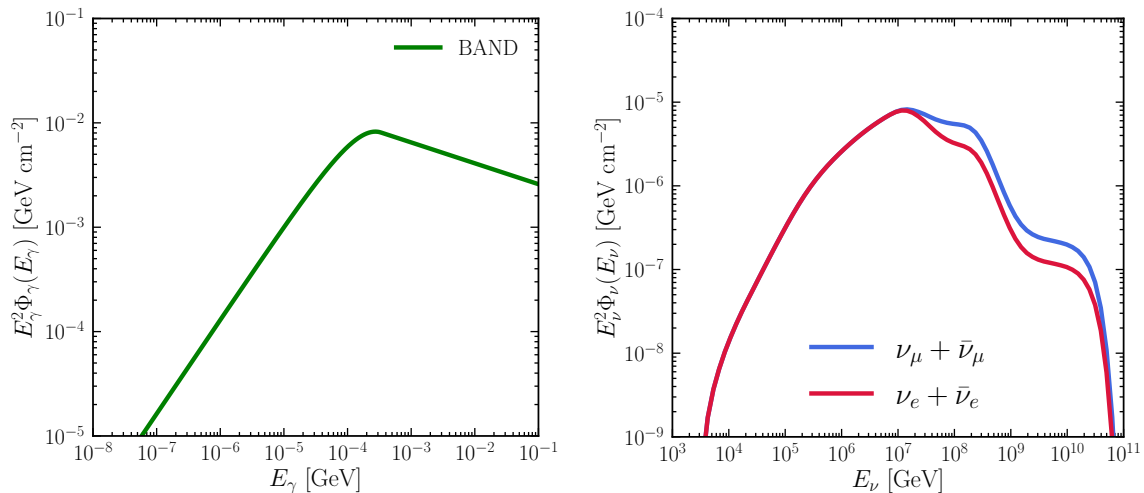


Figure 8. *Left:* Band photon fluence observed at Earth and emitted at $R_{\text{ICMART}} = 10^{15}$ cm for the ICMART model. The parameters of this GRB are reported in Table 1 and $\eta_\gamma = 0.17$. *Right:* Correspondent $\nu_\alpha + \bar{\nu}_\alpha$ fluence in the observer frame in the presence of flavor conversions for the ICMART model (in blue and red for the muon and the electron flavors, respectively). The muon neutrino fluence peaks at $E_\nu^{\text{peak}} = 1.3 \times 10^7$ GeV; the high energy tail of the neutrino distribution shows the double bump structure due to kaon decay.

The neutrino fluence is displayed in the right panel of Fig. 8. The fluence for the muon flavor peaks at $E_\nu^{\text{peak}} = 1.3 \times 10^7$ GeV. Note that the double bump due to kaon decay is clearly visible in the high-energy tail of the energy distribution. This is due to $E'_{p,\text{max}} \sim E'_{K,\text{max}} \sim 2 \times 10^9$ GeV (while $E'_{\pi,\text{max}} \sim 1.2 \times 10^7$ GeV). This feature is determined by the stronger magnetic field in the acceleration region ($B' \simeq 9$ kG, while for example $B' \simeq 1$ kG in the IS model).

5.2.2 Magnetized jet model with gradual dissipation

For the model introduced in Sec. 2.2.2, we follow Ref. [48] and assume that the energy which is dissipated in the optically thick region is reprocessed into quasi-thermal emission, leading to a black-body-like emission from the photosphere. In the optically thin region, the synchrotron radiation from electrons is the dominant emission mechanism and it represents the non-thermal prompt emission. The energy emitted at the photosphere is obtained by integrating the energy dissipation rate (Eq. 2.11) up to R_{PH} and considering that only the fraction $(R/R_{\text{PH}})^{4/9}$ of the energy dissipated at R remains thermal at R_{PH} . In the optically thin region, electrons are always in the fast cooling regime and $E'_{\gamma,\text{ssa}} \gg E'_{\gamma,\text{cool}}$ for $R_{\text{ph}} < R < R_{\text{sat}}$ with our choice of parameters. Here $E'_{\gamma,\text{ssa}}$ is the synchrotron self-absorption energy [49]:

$$E'_{\gamma,\text{ssa}} \sim \left(\frac{h^3}{8\pi m_p} \frac{\xi \tilde{L}_{\text{iso}}}{4\pi \Gamma_{\text{sat}}} \frac{1}{R^2 \Gamma(R)} \right)^{1/3}. \quad (5.8)$$

The shape of the synchrotron spectrum follows Eq. A.10, but we replace E'_{cool} with $E'_{\gamma,\text{ssa}}$ and use $\alpha_\gamma = 1$ for $E'_\gamma < E'_{\gamma,\text{ssa}}$ [49]. Furthermore, only a fraction $\xi = 0.2$ [48] of electrons is accelerated.

For our reference GRB we adopt $\lambda = 4 \times 10^8$ cm [48]. The terminal Lorentz factor of the outflow is $\Gamma_{\text{sat}} \simeq \Gamma_0 \sigma_0$. We choose $\Gamma_{\text{sat}} = 300$ and the initial jet magnetization is $\sigma_0 = \Gamma_{\text{sat}}^{2/3} \sim 45$.

For what concerns protons, we assume that they are accelerated into a power-law distribution starting from a minimum Lorentz factor

$$\gamma'_{p,\text{min}} = \max \left[1, \frac{k_p - 2}{k_p - 1} \frac{\varepsilon_p}{2} \sigma(R) \right] \quad (5.9)$$

and extending up to a maximum value determined by balancing the energy gain and loss rates, as described in Sec. 3.2. We also assume that the power of the proton distribution is the same as the one of electrons, namely $k_p = k_e$ (see Eq. 2.15). The latter assumption is motivated by particle-in-cell simulations of magnetic reconnection for $\sigma \gg 1$ [101], but it has to be yet demonstrated for $\sigma \sim 1$ [99].

We compute the neutrino production assuming that dissipation and particle acceleration start at $R_1 = a R_{\text{PH}}$ with $a = 3$. Being an arbitrary choice for the starting radius, we explore the effects of a on the neutrino fluence in Appendix B. For illustration purposes, we compute the neutrino production rate at three radii (R_1 , R_2 , and R_3) equally distanced in logarithmic scale. We make this choice in order to establish the qualitative trend of the neutrino production during the evolution of the outflow in the optically thin region. The photon and proton distributions are normalized at each radius R_i along the jet to the energy dissipated between R_{i-1} and R_i , where $R_0 = R_{\text{PH}}$ and $R_3 = R_{\text{sat}}$. At each R_i , the photon field coming from R_j is Lorentz transformed through the relative Lorentz factor

$$\Gamma_{\text{rel},ij} = \frac{1}{2} \left(\frac{\Gamma_i}{\Gamma_j} + \frac{\Gamma_j}{\Gamma_i} \right), \quad (5.10)$$

Table 2. Summary table for the input parameters adopted at the radii R_1 , R_2 and R_3 in the magnetic model with gradual dissipation: the radius (R), the comoving magnetic field (B'), the Lorentz factor (Γ), the maximum energy of protons ($E'_{p,\max}$), pions ($E'_{\pi,\max}$), muons ($E'_{\mu,\max}$), and kaons ($E'_{K,\max}$), as well as the power-law slope ($k_e = k_p$) of electrons and protons.

	R [cm]	B' [kG]	Γ	$E'_{p,\max}$ [GeV]	$E'_{\pi,\max}$ [GeV]	$E'_{\mu,\max}$ [GeV]	$E'_{K,\max}$ [GeV]	k_e
R_1	7.1×10^{12}	1.7×10^3	176	1.1×10^8	6.5×10^4	3.6×10^3	7.5×10^6	2.4
R_2	1.6×10^{13}	5.4×10^2	230	1.7×10^8	2×10^5	1.1×10^4	2.3×10^7	2.5
R_3	3.6×10^{13}	1.7×10^2	300	2.5×10^8	6.4×10^5	3.5×10^4	7.3×10^7	2.6

that holds as long as $\Gamma_i, \Gamma_j \gg 1$. The total photon number density used as input at each radius R_i for producing neutrinos is thus

$$n'_{\text{tot}}(E'_\gamma, R_i) = \sum_{j=0}^i \left(\frac{R_j}{R_i} \right)^2 n'_j \left(\frac{E'_\gamma}{\Gamma_{\text{rel},ij}} \right) \frac{1}{\Gamma_{\text{rel},ij}} \quad (5.11)$$

where $n'_j(E'_\gamma)$ is the photon energy distribution at R_j (in units of $\text{GeV}^{-1}\text{cm}^{-3}$).

Once the photon distributions are set, we evaluate the proton cooling times at each radius. In all the three cases, dominant losses are due to the adiabatic cooling up to $\simeq 10^5$ GeV, and $p\gamma$ interactions for $10^5 \text{ GeV} \lesssim E'_p \lesssim E'_{p,\max}$. Synchrotron losses become relevant around 10^7 GeV. Given the very strong magnetic field (see Table 2), the secondaries suffer strong synchrotron losses; this considerably affects the resulting neutrino spectrum, which is damped at energies much lower than in all the other models investigated so far in this work. A summary of the input parameters at the three R_i is reported in Table 2.

The (photon) neutrino fluence at Earth is shown in the (left) right panel of Fig. 9. The slope of the three non-thermal synchrotron components and their distribution peaks decrease as the distance from the source increases. The high energy cut-off of each spectral component is given by Eq. A.1. Notably, the dominant component comes from the smallest radius, while the contribution coming from larger radii gets lower and lower (67%, 26%, and 7% from R_1, R_2 and R_3 , respectively). The significant drop in the neutrino flux between R_1 and R_3 is mainly due to the decrease of the proton power slope (see Table 2), which causes a more pronounced drop in proton number density in the energy range of interest. This is a peculiar feature of this model, which predicts parameters depending on the jet magnetization, and thus changing with the radius.

The neutrino fluence for the muon flavor peaks at $E_\nu^{\text{peak}} = 7.2 \times 10^5$ GeV, which is about $\mathcal{O}(10 - 100)$ GeV smaller than in the models presented in the previous sections, although roughly comparable in intensity at peak. This is due to the fact that, in this case, the main contribution to the neutrino flux comes from the interaction of protons with thermal photons, whose energy peaks at ~ 22 keV. The second bump visible in the spectrum is instead represented by the kaon contribution. Apart from the ICMART model, this is the only other case out of the ones studied in this work in which this feature is clearly identified at higher energies. The reason is the very strong magnetic field in these two magnetic models. Another peculiar feature of this model is the low-energy tail of the neutrino distribution, which is higher than in previous cases. This is due to a combination of the larger number

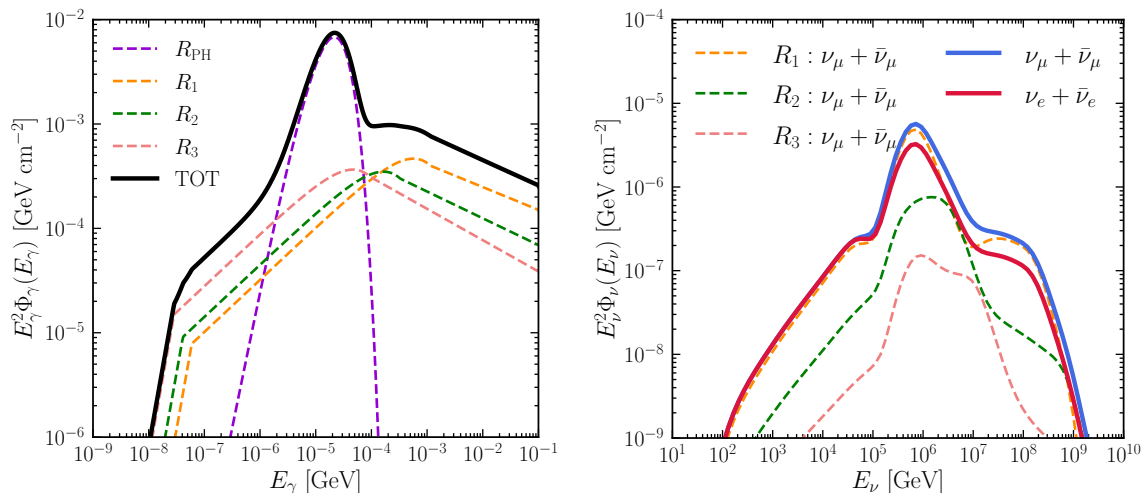


Figure 9. *Left:* Photon fluence in the observer frame for the GRB model invoking continuous magnetic dissipation for the parameters reported in Tables 1 and 2. The total photon energy distribution is shown in black, and its components at R_{PH} , R_1 , R_2 , and R_3 are plotted in violet, orange, green, and coral respectively. *Right:* Correspondent $\nu_\alpha + \bar{\nu}_\alpha$ fluence at Earth after flavor oscillations in the left panel (in blue for the muon flavor and in red for the electron one). The fluence for the muon flavor peaks at $E_\nu^{\text{peak}} = 7.2 \times 10^5$ GeV. An unusual spectral structure is clearly visible.

density [$\mathcal{O}(10^3 - 10^4)$] of protons at low energies in the acceleration region and the extended photon field at higher energies.

5.3 Proton synchrotron model

In order to estimate the neutrino production in the proton synchrotron model (see Sec. 2.3), we need to evaluate the fraction of the proton energy which goes into $p\gamma$ interactions. We consider the photon spectral fit as in Eq. A.10 and follow Ref. [39], which provides the cooling energy $E_{\gamma,\text{cool}}$, the peak energy (or minimum injection energy) $E_{\gamma,\text{peak}} \equiv E_{\gamma,\text{min}}$, and the energy flux at the cooling energy ($F_{\gamma,\text{cool}}$).

Another inferred quantity is the cooling timescale of the radiating particles, $t_{\text{cool}} \sim 1$ s. The cooling time t_{cool} is related, after Lorentz transforming, to the comoving magnetic field B' and γ'_{cool} by means of Eq. A.7. The variability timescale is assumed to be $t_v = 0.5$ s; the duration of the burst, as well as the redshift information, is extracted from the GRB catalog [140]. These observables can be used to constrain the source parameters, such as B' ,

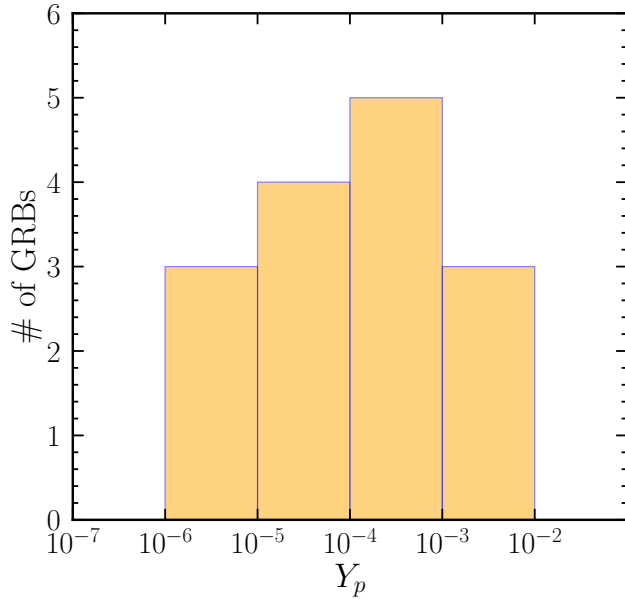


Figure 10. Histogram of Y_p (see Eq. 5.17) for a subset of GRBs analyzed in Ref. [39] for which redshift information is available; $\Gamma = 300$ and $t_v = 0.5$ s are adopted. The parameter Y_p quantifies the relative importance between the proton synchrotron emission and $p\gamma$ interactions. The very low values of Y_p for most of GRBs in the sample suggest a negligible neutrino production of this class of GRBs.

γ'_{\min} , R_γ , Γ , and $E'_{\gamma,\text{bol,iso}}$ through the following relations [39]:

$$E_{\gamma,\text{peak}} = \frac{3 \hbar e B' \gamma'^2_{\min}}{2 m_p c} \frac{\Gamma}{1+z}, \quad (5.12)$$

$$E_{\gamma,\text{cool}} = \left(\frac{m_p}{m_e}\right)^5 \frac{54 \pi^2 \hbar e m_e c}{\sigma_T^2 B'^3 t_{\text{cool}}^2} \frac{1+z}{\Gamma}, \quad (5.13)$$

$$F_\gamma = F_{\gamma,\text{cool}} \left(\frac{E_{\gamma,\text{cool}}}{h}\right) \left[\frac{3}{4} + 2 \sqrt{\frac{E_{\gamma,\text{peak}}}{E_{\gamma,\text{cool}}}} - 2 + \frac{2}{k_p - 2} \sqrt{\frac{E_{\gamma,\text{peak}}}{E_{\gamma,\text{cool}}}} \right], \quad (5.14)$$

$$E'_{\gamma,\text{bol,iso}} = \frac{4\pi d_L^2(z) F_\gamma t_{\text{dur}}}{\Gamma(1+z)}, \quad (5.15)$$

$$R_\gamma = \frac{2ct_v \Gamma^2}{(1+z)}. \quad (5.16)$$

where $F_\gamma = \tilde{L}_{\gamma,\text{bol,iso}}/4\pi d_L^2(z)$ is the bolometric isotropic radiative flux (in units of $\text{GeV cm}^{-2} \text{s}^{-1}$), $\tilde{L}_{\gamma,\text{bol,iso}}$ being the bolometric isotropic luminosity of the burst over the whole energy range. Using these relations we can infer B' , γ'_{\min} , R_γ and $E'_{\gamma,\text{bol,iso}}$ as functions of Γ .

In order to figure out the relative importance between proton synchrotron and $p\gamma$ cooling for the sample of GRBs studied in Ref. [39], we introduce the following parameter [141]:

$$Y_p \equiv \frac{L'_{p,p\gamma}}{L'_{p,\text{syn}}} \approx \frac{\sigma_{p\gamma}}{\sigma_{p,T}} \frac{U'_{p,\text{syn}}}{U'_B} = \frac{\sigma_{p\gamma}}{\sigma_{p,T}} \frac{E'_{\gamma,\text{tot,iso}}}{V'_{\text{iso}}} \frac{8\pi}{B'^2} = \frac{\sigma_{p\gamma}}{\sigma_{p,T}} \frac{8\pi F_\gamma d_L^2(z)}{\Gamma^2 R_\gamma^2 c B'^2}, \quad (5.17)$$

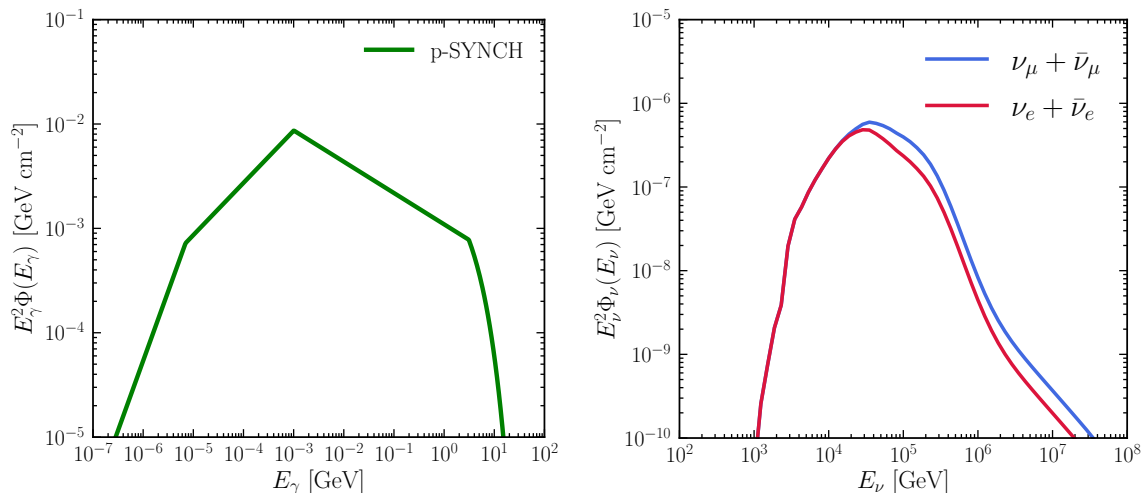


Figure 11. *Left:* Photon fluence in the observer frame for the proton synchrotron model; see Table 1 for the model parameters, in addition $\tilde{E}_{\gamma,\text{iso}} = 5 \times 10^{53}$ ergs, $t_{\text{cool}} = 0.5$ s, $\gamma_{\text{min}}/\gamma_{\text{cool}} = 12$, $E_{\gamma,\text{cool}} = 7$ keV. *Right:* Correspondent $\nu_{\alpha} + \bar{\nu}_{\alpha}$ fluence (in red and blue for the electron and muon flavors, respectively). The peak in the neutrino distribution ($E_{\nu}^{\text{peak}} = 3.5 \times 10^4$ GeV), due to the cooling energy break $E_{\gamma,\text{cool}}$, is shifted to lower energies with respect to the other analyzed models. The damping at high energies is due to the very strong magnetic field in the emitting region ($B' \simeq 8.5 \times 10^6$ G).

where $L'_{p,p\gamma}$ and $L'_{p,\text{sync}}$ are the proton energy loss rates for $p\gamma$ interactions and synchrotron emission respectively, and $\sigma_{p,\Gamma} = \sigma_{\text{T}}(m_e/m_p)^2$. By relying on Eqs. 5.13 and 5.16, Y_p can be estimated as a function of the bulk Lorentz factor.

For our benchmark $\Gamma = 300$, we compute Y_p for the GRBs studied in Ref. [39] for which redshift information is available. The histogram of Y_p is shown in Fig. 10. We can see that Y_p spreads over almost three orders of magnitude, with very low typical values. Hence, assuming proton synchrotron radiation as the main emission mechanism, we expect this class of GRBs to be poor emitters of high energy neutrinos. To show this quantitatively, we compute the neutrino fluence for our representative GRB.

We adopt the following GRB parameters: $\gamma_{\text{min}}/\gamma_{\text{cool}} = 12$, $E_{\gamma,\text{cool}} = 7$ keV, $\Gamma = 300$, $z = 2$, $E_{\gamma,\text{peak}} = (\gamma_{\text{min}}/\gamma_{\text{cool}})^2 E_{\gamma,\text{cool}}$, which result in $\tilde{E}_{\gamma,\text{bol,iso}} \simeq 7 \times 10^{53}$ erg. These values are compatible with the average ones inferred from the sample considered in Ref. [39], namely $\langle \tilde{E}_{\gamma,\text{bol,iso}} \rangle \simeq 7.4 \times 10^{53}$ erg, $\langle E_{\gamma,\text{cool}} \rangle \simeq 6.4$ keV, and $\langle \gamma_{\text{min}}/\gamma_{\text{cool}} \rangle \simeq 11.9$. Furthermore, we choose $k_p = 2.6$ for the slope of the injection proton spectrum $Q'(\gamma'_p)$, that reproduces the typical value of the high energy photon index $\beta \sim -2.3$; note that k_p is almost never constrained for the sample in Ref. [39].

As for the radiated energy, this fiducial GRB is comparable to the ones analyzed in the previous sections, except for the total energetics. In fact, given the very high magnetic field, $B' \simeq 8.5 \times 10^6$ G, the total isotropic energy is $\tilde{E}_{B,\text{iso}} \propto R_{\gamma}^2 \Gamma B'^2 \sim \mathcal{O}(10^{60})$ erg, much larger than the typical energy that a GRB jets is able to release (spin down of magnetars or through the Blandford-Znajek mechanism [10]). Since the synchrotron radiation dominates by many orders of magnitude over all the other proton energy loss mechanisms, we assume $U'_{p,\text{iso}} \simeq E'_{\gamma,\text{bol,iso}}$, where U'_p is the total isotropic proton energy in the comoving frame. Such a jet turns out to be highly inefficient in radiating energy, given that $\tilde{E}_{\text{iso}} \sim \tilde{E}_{B,\text{iso}} \gg \tilde{E}_{\gamma,\text{bol,iso}}$.

By considering the proton energy distribution as in Eq. A.10 and normalizing it to U'_p , we compute the neutrino fluence and show it in the right panel of Fig. 11. The left of the same figure shows the total synchrotron photon fluence. Analogously to the model in Sec. 5.2.2, the peak in the neutrino distribution ($E_\nu^{\text{peak}} = 3.5 \times 10^4$ GeV) is due to the cooling energy break $E_{\gamma,\text{cool}}$ and it is shifted to lower energies. The neutrino spectrum is furthermore strongly damped at high energies due to the synchrotron cooling of mesons in the jet. Our estimation of the neutrino emission results to be in agreement with the one reported in the independent work of Ref. [51], for GRBs with similar parameters.

The proton synchrotron model, besides requiring unreasonable total jet energies, predicts the smallest neutrino fluence among all models considered in this work. We note that with the choice made of parameters, our representative GRB has $Y_p \sim \mathcal{O}(10^{-4})$; hence, our estimation may be considered an optimistic one, given the distribution of Y_p shown in Fig. 10. We refer the interested reader to Ref. [51] for additional details and discussion on this model.

6 Discussion

In this work, we have computed the neutrino fluence for a class of models adopted to describe the prompt phase of long GRBs, all having the same \tilde{E}_{iso} . Because of the diversity of electromagnetic GRB data and the uncertainties inherent to the models (e.g., jet composition, energy dissipation mechanism, particle acceleration, and radiation mechanisms), an exhaustive theoretical explanation of the mechanism powering GRBs is still lacking. To compare the neutrino production across models, we have selected input parameters for a benchmark GRB motivated by observations. In addition, the modeling of the dissipative and acceleration efficiencies, as well as the properties of the accelerated particle distributions have been guided by the most recent simulation findings. A summary of our input parameters is reported in Table 1. In this section, we compare the energetics of the GRB models explored in this work as well as the detection prospects of stacked neutrino fluxes.

6.1 Energetics

A summary of our findings is reported in Table 3, where the radiative efficiency of the jet (Eq. 3.1) is listed for the six GRB models investigated in this paper together with the isotropic photon and neutrino (for six flavors) energies, as well as the ratio of the latter two. As already discussed in Sec. 5, the least efficient model in converting \tilde{E}_{iso} in $\tilde{E}_{\gamma,\text{iso}}$ is the proton synchrotron model, whilst the most efficient one is the model which considers a dissipative photosphere as the main source of prompt emission. This is mainly due to the high dissipative efficiency suggested by recent three-dimensional simulations [86]. Note that the radiative efficiency is an input parameter of each model, since we do not compute the radiation spectra self-consistently.

Among the models considered in this work, all with identical \tilde{E}_{iso} , neutrinos carry the largest amount of energy in the ICMART model; the jet model with a dissipative photosphere and the jet model with three emission components have very similar $\tilde{E}_{\nu,\text{iso}}$.

The reason for such a high neutrino yield in these three cases lies in the large photon number density in the acceleration region. Indeed, although the model with three components presents a slightly smaller $E_{\gamma,\text{iso}}$, the high $E_{\nu,\text{iso}}$ is due to the fact that protons interact with a high-energy photon component comparable in intensity to the one in the γ -ray range (i.e. 1 keV – 10 MeV). This leads to an enhancement in the neutrino flux by a factor of ~ 2 with respect to the IS model, for example, where the number density of photons above 10 MeV is

negligible. This also explains the trend for $\tilde{E}_{\nu,\text{iso}}/\tilde{E}_{\gamma,\text{iso}}$ reported in Table 3 (note that $\tilde{E}_{\gamma,\text{iso}}$ in Table 3 is estimated over the energy range 1 keV – 10 MeV; hence, this ratio, when defined with the bolometric photon energy used for neutrino production, should be slightly smaller than the one reported for the IS model with a dissipative photosphere, the model with three components, the magnetic one with gradual dissipation, and the proton synchrotron model).

6.2 Detection perspectives

In order to compare the neutrino detection perspectives for our six models, we compute the all-sky quasi-diffuse flux for neutrinos and antineutrinos. We assume that our benchmark GRB at $z = 2$ yields a neutrino emission that is representative of the entire GRB population. For $\dot{N} \simeq 667 \text{ yr}^{-1}$ long GRBs per year [32], the stacking flux for the muon flavor over the whole sky is defined as

$$F_{\nu_\mu}(E_\nu) = \frac{1}{4\pi} \dot{N} \Phi_{\nu_\mu}(E_\nu, z = 2). \quad (6.1)$$

Figure 12 shows the resultant all-sky quasi-diffuse fluxes for the muon flavor for the six GRB models as functions of the neutrino energy (colored curves). For comparison, we also show the GRB staking limits of IceCube [32] and the projected ones for IceCube-Gen2 [142] (black curves). In agreement with the non-detection of high-energy neutrinos from targeted GRB searches [32], our forecast for the neutrino fluxes lies below the experimental limits and is in agreement with the upper limits reported by the ANTARES Collaboration [31] and with the ones expected for KM3NeT [143]. All considered models predict comparable neutrino flux at peak energy, except for the IS model and the proton synchrotron one (see also Table 3).

An important aspect to consider in targeted GRB searches is the large spread in energy and shape of the expected neutrino fluxes for different jet models. It is evident from Fig. 12 that the neutrino flux peak energy ranges from $\mathcal{O}(10^4)$ GeV for the proton synchrotron model

Table 3. Summary of the derived quantities for the models considered in this work and our benchmark parameters value (see Table 1). The radiative efficiency of the jet (Eq. 3.1), the isotropic photon energy in the 1 keV–10 MeV energy range, the isotropic neutrino energy for neutrinos and antineutrinos of all flavors, the ratio between the isotropic total neutrino and photon energies, the neutrino energy at the fluence peak, and the maximum proton energy are listed. The model with the smallest radiative efficiency is the proton synchrotron model; this model has also the smallest $\tilde{E}_{\nu,\text{iso}}$. The most radiatively efficient model is the one with a dissipative photosphere; while $\tilde{E}_{\nu,\text{iso}}$ is comparable among the jet model with a dissipative photosphere, the one with three emission components, and the ICMART model.

<i>Model</i>	η_γ (%)	$\tilde{E}_{\gamma,\text{iso}}$ [erg]	$\tilde{E}_{\nu,\text{iso}}$ [erg]	$\tilde{E}_{\nu,\text{iso}}/\tilde{E}_{\gamma,\text{iso}}$	$E_{\nu_\mu}^{\text{peak}}$ [GeV]	$E_{p,\text{max}}$ [GeV]
IS	1.7	5.7×10^{52}	6.2×10^{50}	1.1×10^{-2}	3.6×10^7	5.5×10^{10}
PH-IS	20	6.8×10^{53}	1.4×10^{51}	2.1×10^{-3}	6.4×10^7	1.2×10^{10}
3-COMP	2.1	7.2×10^{52}	1.2×10^{51}	1.6×10^{-2}	4×10^7	5.4×10^{10}
ICMART	17.5	6×10^{53}	1.8×10^{51}	3×10^{-3}	1.3×10^7	1.7×10^{11}
MAG-DISS	8	2.7×10^{53}	5.2×10^{50}	2×10^{-3}	7.2×10^5	2.5×10^{10}
p-SYNCH	2×10^{-5}	5×10^{53}	7×10^{49}	1.4×10^{-4}	3.5×10^4	6.9×10^9

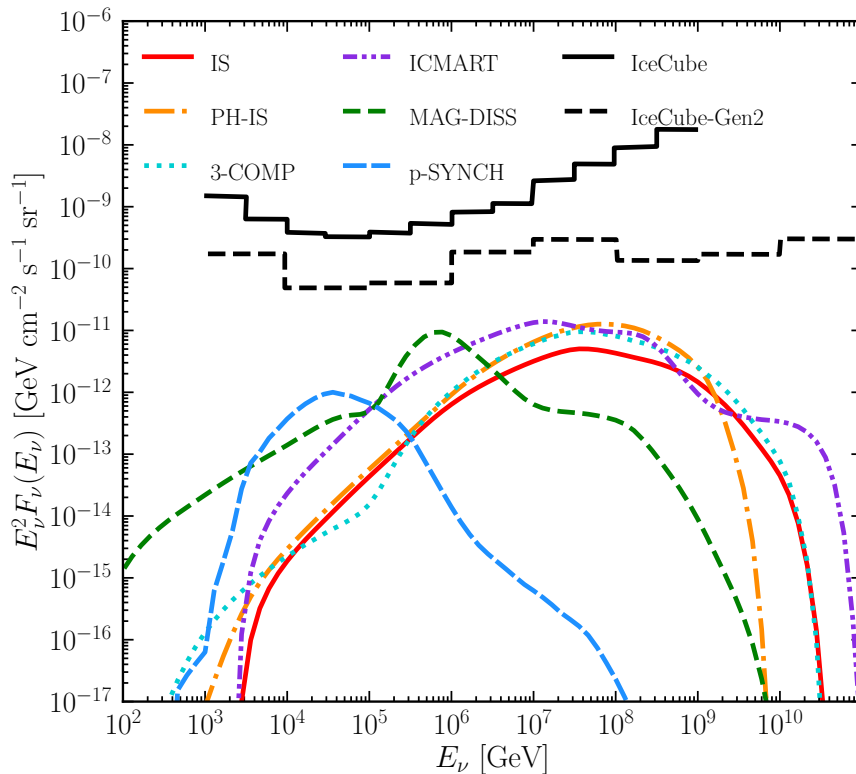


Figure 12. Model comparison of the expected all-sky quasi-diffuse fluxes for the six GRB models considered in this work for the benchmark jet parameters listed in Table 1. The quasi-diffuse flux has been computed by relying on Eq. 6.1 for $\nu_\mu + \bar{\nu}_\mu$; all models have identical \tilde{E}_{iso} . For comparison, the IceCube staking limits (combined analysis for 1172 GRBs) [32] and the expected sensitivity for IceCube-Gen2 (based on a sample of 1000 GRBs) [142] are reported (solid and dashed black lines). By relying on the most up-to-date best-fit GRB parameters, all models predict a quasi-diffuse flux that lies below the sensitivity curves; however, a large spread in energy and shape of the expected neutrino fluxes is expected for different jet models.

to $\mathcal{O}(10^8 - 10^9)$ GeV for the IS model with a dissipative photosphere. As such, targeted searches assuming one specific GRB model, such as the IS one, as benchmark case for the GRB neutrino emission may lead to biased results.

It is worth noticing that our predictions rely on best fit values of the input parameters and assume one GRB as representative of the whole population. Variations of the jet parameters within their uncertainty range could lead to variations of the expected neutrino flux up to a couple of orders of magnitude, see e.g. Refs. [36, 73], possibly hitting the IceCube-Gen2 sensitivity. In addition, since none of the considered jet models can account for all observational constraints, a population study [42] may further affect the expected quasi-diffuse emission.

Another caveat of our modeling is that the spectral energy distributions of photons and the ones of the secondary particles produced through $p\gamma$ interactions are not computed self-consistently; this may affect the overall expected emission, see e.g. Refs. [144–148] for dedicated discussions.

7 Conclusions

Long duration gamma-ray bursts (GRBs) are subject of investigation since long time, being among the most mysterious transients occurring in our universe. In the attempt of explaining the observed electromagnetic GRB emission, various models have been proposed. The main goal of this work is to show that the neutrino emission strongly depends on the chosen jet model, despite the fact that different jet models may be equally successful in fitting the observed electromagnetic spectral energy distributions.

To this purpose, we choose a benchmark GRB and compute the neutrino emission for kinetic dominated jets, i.e. in the internal shock model, also including a dissipative photosphere as well as three spectral components. We also consider Poynting flux dominated jets: a jet model invoking internal-collision-induced magnetic reconnection and turbulence (ICMART) and a magnetic jet model with gradual dissipation. A jet model with dominant proton synchrotron radiation in the keV-MeV energy range is also taken into consideration. In particular, the neutrino production for the latter two models has been investigated for the first time in this work.

Defining the radiative efficiency as the ratio of isotropic gamma-ray energy to the total isotropic energy of the jet, we find that the least radiatively efficient model is the proton synchrotron one, while the most efficient one is the model with a dissipative photosphere. However, the model predicting the largest amount of isotropic-equivalent energy going into neutrinos is the ICMART one.

In the context of targeted searches, it should be noted that the expected quasi-diffuse neutrino flux can vary up to 1–1.5 orders of magnitude in amplitude and peak at energies ranging from 10^4 to 10^8 GeV. The predicted spectral shape of the neutrino distribution is also strongly dependent on the adopted jet model. A summary of our findings is reported in Table 3 and Fig. 12.

This work highlights the great potential of neutrinos in pinpointing the GRB emission mechanism in the case of successful neutrino detection. In particular, it suggests the need to rely on a wide range of jet models in targeted stacking searches.

Note added: The modeling of the neutrino emission for the proton synchrotron model is also presented in the independent work of Ref. [51]. Our paper focuses on the comparison of the neutrino production across different GRB models for the prompt emission, while Ref. [51] investigates the plausibility of the proton synchrotron interpretation.

Acknowledgments

We are grateful to Jochen Greiner and Gor Oganesyan for insightful discussions. This project has received funding from the Villum Foundation (Project No. 13164), the Carlsberg Foundation (CF18-0183), the Knud Højgaard Foundation, the Deutsche Forschungsgemeinschaft through Sonderforschungsbereich SFB 1258 “Neutrinos and Dark Matter in Astro- and Particle Physics” (NDM), and the MERAC Foundation.

A Spectral energy distributions of photons: fitting functions

In order to describe the electromagnetic emission, in this appendix we introduce the main spectral functions used to fit the electromagnetic data: the Band function, the cut-off power-

law, a simple power-law, and a double broken power-law usually representing the synchrotron emission from a marginally fast cooling particle population. The various spectral functions introduced here are then employed to model the GRB emission in Sec. 5.

When the energy distribution does not present an intrinsic cut-off at high energies (e.g., Band function and synchrotron spectrum), we define $E'_{\gamma,\text{cutoff}}$ as the energy at which the opacity to photon-photon pair production becomes unity

$$\tau_{\gamma\gamma}(E'_{\gamma,\text{cutoff}}) \simeq 0.1\sigma_T E'_* n'_\gamma(E'_*) \frac{R_\gamma}{2\Gamma} = 1 \quad (\text{A.1})$$

where $E'_* = m_e^2 c^4 / E'_{\gamma,\text{cutoff}}$ and $\tau_{\gamma\gamma}(E'_{\gamma,\text{cutoff}})$ is the opacity for the photons with energy $E'_{\gamma,\text{cutoff}}$ and number density distribution $n'_\gamma(E'_\gamma)$.

A.1 Band function

The Band function [149] is the most used empirical function to fit the time-integrated electromagnetic spectra. Despite fitting well the data, it is still lacking a clear physical meaning. It consists of a smoothly joint broken power-law:

$$n_\gamma^{\text{Band}}(E_\gamma) = C \begin{cases} \left(\frac{E_\gamma}{100 \text{ keV}}\right)^{\alpha_\gamma} \exp\left[-\frac{(\alpha_\gamma+2)E_\gamma}{E_{\gamma,p}}\right] & E_\gamma < E_{\gamma,c} \\ \left(\frac{E_\gamma}{100 \text{ keV}}\right)^{\beta_\gamma} \exp(\beta_\gamma - \alpha_\gamma) \left(\frac{E_{\gamma,c}}{100 \text{ keV}}\right)^{\alpha_\gamma - \beta_\gamma} & E_\gamma \geq E_{\gamma,c} \end{cases} \quad (\text{A.2})$$

where

$$E_{\gamma,c} = \left(\frac{\alpha_\gamma - \beta_\gamma}{\alpha_\gamma + 2}\right) E_{\gamma,\text{peak}}, \quad (\text{A.3})$$

C is a normalization constant (in units of $\text{GeV}^{-1} \text{cm}^{-3}$), α_γ and β_γ are the low-energy and high-energy power-law photon indices, $E_{\gamma,c}$ represents the energy where the low-energy power-law with an exponential cutoff ends and the pure high energy power-law begins. The peak energy $E_{\gamma,\text{peak}}$ is chosen to satisfy the Amati relation [150]:

$$\tilde{E}_{\gamma,\text{peak}} = 80 \left(\frac{\tilde{E}_{\gamma,\text{iso}}}{10^{52} \text{ erg}}\right)^{0.57} \text{ keV}. \quad (\text{A.4})$$

The typical spectral parameters inferred from observations are: $\alpha_\gamma \simeq -1.1$, $\beta_\gamma \simeq -2.2$, and $E_{\gamma,\text{peak}} \simeq 300 \text{ keV}$ [2].

A.2 Cut-off power-law

Although the Band spectrum is the best fitting function for most GRBs, it has been shown that in some cases a cut-off power-law (CPL) can represent the preferred model [151–153]. The CPL is a power-law model with a high energy exponential cut-off :

$$n_\gamma^{\text{CPL}}(E_\gamma) = C \left(\frac{E_\gamma}{100 \text{ keV}}\right)^{\alpha_\gamma} \exp\left[-\frac{(\alpha_\gamma + 2)E_\gamma}{E_{\gamma,\text{peak}}}\right], \quad (\text{A.5})$$

where α_γ is the photon index and $E_{\gamma,\text{peak}}$ the peak energy, whose value will be specified later. In an optically thick thermal scenario, $\alpha_\gamma = 1$ in the Rayleigh-Jeans limit, $\alpha_\gamma = 2$ in the Wien limit, $\alpha_\gamma = 0.4$ for a non-dissipative photosphere in the coasting phase and $\alpha_\gamma < 0$ for all non-thermal emissions [41].

A.3 Power law

In the cases of faint bursts or narrow detector bandpass, the whole GRB spectrum, or one of its components, can be fitted with a simple power-law [154] defined as

$$n_{\gamma}^{\text{PL}}(E_{\gamma}) = C \left(\frac{E_{\gamma}}{100 \text{ keV}} \right)^{\alpha_{\gamma}}, \quad (\text{A.6})$$

where C is the normalization and α_{γ} is the power-law photon index.

A.4 Double broken power law

This is a spectral model that is commonly adopted to describe the synchrotron emission of a fast cooling population of particles that are being injected into the emitting region with a power-law distribution at a rate $Q(\gamma) \propto \gamma^{-k}$ with $\gamma_{\min} < \gamma < \gamma_{\max}$. During an emission period t , the charged particles of mass m lose most of their energy above the characteristic value γ_{cool} :

$$\gamma_{\text{cool}}(t) = \frac{6\pi mc}{\sigma_{\text{T}}\beta^2 B^2 t} \left(\frac{m}{m_e} \right)^2, \quad (\text{A.7})$$

where m_e is the electron mass. Considering a constant injection rate of particles in the emitting region which radiate in the fast cooling regime ($\gamma_{\min} > \gamma_{\text{cool}}$) at a rate $\propto \gamma^2$, after a time t the emitting particle distribution has the following shape [68]:

$$n(\gamma, t) \propto \begin{cases} 0 & \gamma < \gamma_{\text{cool}} \text{ and } \gamma > \gamma_{\max} \\ \gamma^{-2} & \gamma_{\text{cool}} < \gamma < \gamma_{\min} \\ \gamma^{-(k+1)} & \gamma_{\min} < \gamma < \gamma_{\max} \end{cases}. \quad (\text{A.8})$$

Given that each particle radiates photons with a characteristic synchrotron energy

$$E_{\gamma}(\gamma) = \frac{3}{2} \frac{\hbar e}{mc} \gamma^2 B, \quad (\text{A.9})$$

the particle distribution in Eq. A.8 emits the following synchrotron spectrum:

$$n_{\gamma}^{\text{sync}}(E_{\gamma}) = C \begin{cases} \left(\frac{E_{\gamma}}{E_{\gamma, \text{cool}}} \right)^{-\frac{2}{3}} & E_{\gamma} < E_{\gamma, \text{cool}} \\ \left(\frac{E_{\gamma}}{E_{\gamma, \text{cool}}} \right)^{-\frac{3}{2}} & E_{\gamma, \text{cool}} < E_{\gamma} < E_{\gamma, \text{min}} \\ \left(\frac{E_{\gamma, \text{min}}}{E_{\gamma, \text{cool}}} \right)^{-\frac{3}{2}} \left(\frac{E_{\gamma}}{E_{\gamma, \text{min}}} \right)^{-\frac{k+2}{2}} & E_{\gamma, \text{min}} < E_{\gamma} < E_{\gamma, \text{max}} \end{cases}, \quad (\text{A.10})$$

where $E_{\gamma, \text{cool}}$, $E_{\gamma, \text{min}}$, and $E_{\gamma, \text{max}}$ correspond to the characteristic photon energies mainly emitted by particles with gamma factors γ_{cool} , γ_{\min} , and γ_{\max} , respectively.

B Magnetized jet model with gradual dissipation: dependence of the neutrino emission on the input parameters

One of the main, but less certain, parameters of the jet model with gradual magnetic dissipation is the initial magnetization σ_0 . This, in turn, determines the photospheric radius, the saturation Lorentz factor, the energy dissipation rate, and other parameters. For this reason, we investigate the impact of σ_0 on the photon and neutrino fluences by considering

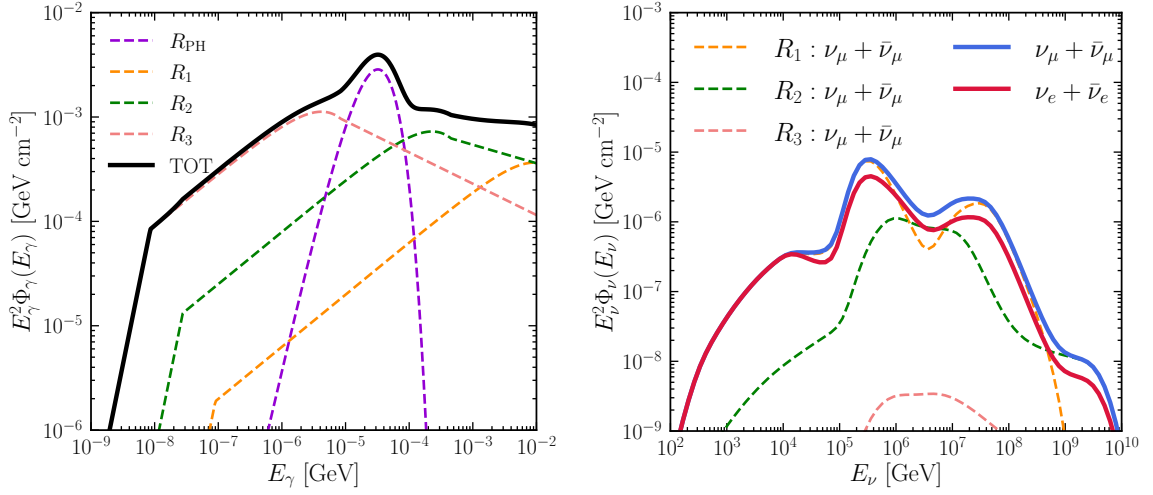


Figure 13. Similar to Fig. 9, but for $\sigma_0 = 100$. The fluence for the muon flavor peaks at $E_\nu^{\text{peak}} = 3.3 \times 10^5$ GeV. In addition, $E_{\nu,\text{iso}} = 8.6 \times 10^{50}$ erg, $E_{\gamma,\text{iso}} = 2.3 \times 10^{53}$ erg, $\Gamma_{\text{sat}} = 1000$, $\sigma_0 = 100$, $R_{\text{PH}} = 7.1 \times 10^{11}$ cm, $R_1 = 2.1 \times 10^{12}$ cm, $R_2 = 3 \times 10^{13}$ cm, $R_3 = 4 \times 10^{14}$ cm, $\Gamma_1 = 180$, $\Gamma_2 = 422$, $\Gamma_3 = 1000$, $\tilde{E}_{\nu,\text{iso}}/\tilde{E}_{\gamma,\text{iso}} = 3.7 \times 10^{-3}$, $\eta_\gamma = 7\%$.

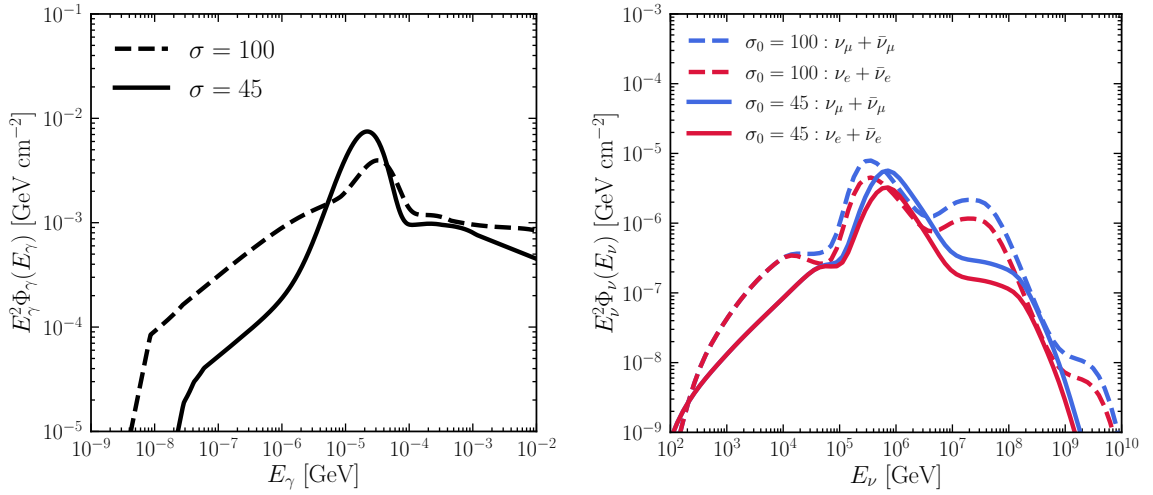


Figure 14. *Left:* Total photon fluence in the observer reference frame, obtained as the sum of the components produced at R_{PH} , R_1 , R_2 and R_3 for the $\sigma_0 = 45$ (solid line) and $\sigma_0 = 100$ (dashed line) cases, respectively. *Right:* Correspondent $\nu_\alpha + \bar{\nu}_\alpha$ fluence (in red and in blue for the electron and muon flavors, respectively). For parameters used, see captions of Figs. 9 and 13.

a case with $\sigma_0 = 100$. All the other parameters, like \tilde{E}_{iso} , are identical to the ones adopted in Sec. 5.2.2. We follow the same procedure to calculate the neutrino flux as outlined in Sec. 5.2.2.

In Fig. 13, we show snapshots of the photon fluence (left panel) and neutrino fluence (right panel) for $\sigma_0 = 100$ at three indicative radii. A comparison between the $\sigma_0 = 45$ and $\sigma_0 = 100$ cases is shown in Fig. 14. A noticeable difference is appreciable between the photon spectral energy distributions. As the initial magnetization increases, the saturation Lorentz

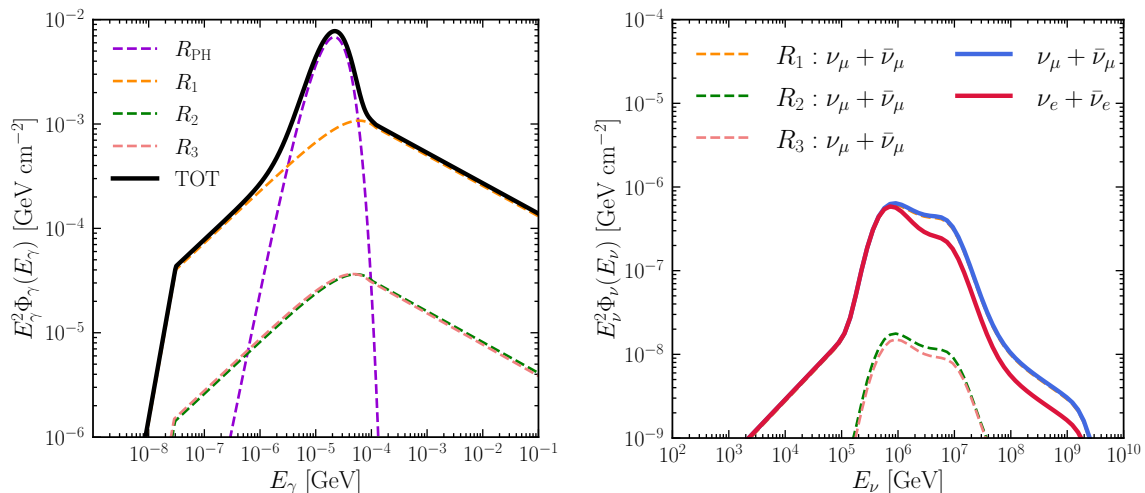


Figure 15. *Left:* Total photon fluence in the observer reference frame, obtained as the sum of the components produced at R_{PH} , R_1 , R_2 and R_3 for the $\sigma_0 = 45$ and $a = 13$ case. *Right:* Correspondent $\nu_\alpha + \bar{\nu}_\alpha$ fluence (in red and in blue for the electron and muon flavors, respectively).

factor increases, namely $\Gamma_{\text{sat}} = \sigma_0^{3/2} = 1000$ for $\sigma_0 = 100$. The energy is dissipated at a rate $\dot{E} \propto R^{1/3}$, while the photosphere occurs at a smaller distance from the source ($R_{\text{PH}} \propto 1/\Gamma_{\text{sat}}$). As a result, less energy is dissipated during the optically thick regime (most of the energy is dissipated at $R > R_{\text{PH}}$) and the photospheric emission becomes dimmer (compare dashed and solid lines at $E_\gamma \sim 10^{-5}$ – 10^{-4} GeV in Fig. 14). The characteristic synchrotron energy $E_{\gamma,\text{min}} \propto \Gamma_{\text{min}}^2 B'$ (Eq. A.9) decreases with the radius (see, e.g., dashed colored curves in the left panel of Fig. 13), while the normalization of the synchrotron photon spectra increases with respect to the case of $\sigma_0 = 45$ (see dashed curve in the left panel of Fig. 14) because of the higher dissipation rate (Eq. 2.11). For a higher σ_0 , particle acceleration begins at smaller radii and so does the production of neutrinos. Moreover, the power slopes of the electron and proton distributions (accelerated via reconnection) are harder [100, 101] because of the higher magnetization in the acceleration region. Because of the larger saturation radius ($R_{\text{sat}} \propto \Gamma_{\text{sat}}^2$) found for higher σ_0 , the dissipated energy up to $R_1 = aR_{\text{ph}} \propto \Gamma_{\text{sat}}^{-1}$ that is available for relativistic particles is less than in the case of lower initial magnetizations. The combination of a smaller amount of dissipated energy up to a given radius, smaller volume and harder proton power slope leads to a neutrino flux at peak (whose main contribution comes from R_1) comparable to the one with $\sigma_0 = 45$ (see right panel of Fig. 14).

For the case of $\sigma_0 = 100$, the second bump in the neutrino spectrum has a fluence that is comparable to the one of the first bump at $\sim 10^6$ GeV. On the contrary, the second bump is barely visible in the neutrino energy distribution with $\sigma_0 = 45$ (compare solid and dashed lines in the right panel of Fig. 14). This is because in the $\sigma_0 = 100$ case, pions suffer stronger synchrotron losses, hence the neutrino intensity resulting from the decay of pions decreases to the level of the one produced by kaons. This is also the reason for a slight shift in the neutrino flux peak to lower energies. Another noticeable feature is the low energy tail. The latter turns out to be higher in the $\sigma_0 = 100$ case, given the higher number density of photons at higher energies.

Finally, in order to explore the effects of the arbitrary choice of the parameter a , we considered the case with $\sigma_0 = 45$ and $a = 13$, where $R_1 \sim R_{\text{sat}}$, see Fig. 15. Since most of

the energy is dissipated within R_1 , the neutrino contribution from R_1 is dominant, although lower by a factor $\mathcal{O}(10)$ if compared to the case with $a = 3$. However, since the case $a = 13$ represents an extreme case, such that all the energy is locally dissipated near the saturation radius, the fluence of $\mathcal{O}(10^{-6})$ GeVcm $^{-2}$ should be considered as the lower limit for the neutrino production from a GRB described by the magnetic model with gradual dissipation for the specific set of parameters adopted in this work.

References

- [1] R. W. Klebesadel, I. B. Strong and R. A. Olson, *Observations of Gamma-Ray Bursts of Cosmic Origin*, *Astrophys. J. Lett.* **182** (1973) L85–L88.
- [2] D. Gruber et al., *The Fermi GBM Gamma-Ray Burst Spectral Catalog: Four Years Of Data*, *Astrophys. J. Suppl.* **211** (2014) 12, [[1401.5069](#)].
- [3] S. E. Woosley, *Gamma-ray bursts from stellar mass accretion disks around black holes*, *Astrophys. J.* **405** (1993) 273.
- [4] A. MacFadyen and S. Woosley, *Collapsars: Gamma-ray bursts and explosions in ‘failed supernovae’*, *Astrophys. J.* **524** (1999) 262, [[astro-ph/9810274](#)].
- [5] S. Woosley and J. Bloom, *The Supernova Gamma-Ray Burst Connection*, *Ann. Rev. Astron. Astrophys.* **44** (2006) 507–556, [[astro-ph/0609142](#)].
- [6] J. Atteia, V. Heussaff, J. P. Dezalay, A. Klotz, D. Turpin, A. Tsvetkova et al., *The maximum isotropic energy of gamma-ray bursts*, *Astrophys. J.* **837** (2017) 119, [[1702.02961](#)].
- [7] M. Petropoulou, P. Beniamini, G. Vasilopoulos, D. Giannios and R. Barniol Duran, *Deciphering the properties of the central engine in GRB collapsars*, *Mon. Not. Roy. Astron. Soc.* **496** (Aug., 2020) 2910–2921, [[2006.07482](#)].
- [8] W.-X. Chen and A. M. Beloborodov, *Neutrino-Cooled Accretion Disks around Spinning Black Hole*, *Astrophys. J.* **657** (2007) 383–399, [[astro-ph/0607145](#)].
- [9] W.-H. Lei, B. Zhang, X.-F. Wu and E.-W. Liang, *Hyperaccreting Black Hole as Gamma-Ray Burst Central Engine. II. Temporal Evolution of the Central Engine Parameters during the Prompt and Afterglow Phases*, *Astrophys. J.* **849** (2017) 47, [[1708.05043](#)].
- [10] R. D. Blandford and R. L. Znajek, *Electromagnetic extractions of energy from Kerr black holes*, *Mon. Not. Roy. Astron. Soc.* **179** (1977) 433–456.
- [11] V. V. Usov, *On the nature of nonthermal radiation from cosmological gamma-ray bursters*, *Mon. Not. Roy. Astron. Soc.* **267** (1994) 1035, [[astro-ph/9312024](#)].
- [12] B. Paczynski, *Gamma-ray bursters at cosmological distances*, *Astrophys. J. Lett.* **308** (1986) L43–L46.
- [13] G. Drenkhahn and H. Spruit, *Efficient acceleration and radiation in Poynting flux powered GRB outflows*, *Astron. Astrophys.* **391** (2002) 1141, [[astro-ph/0202387](#)].
- [14] P. Mészáros, *Astrophysical Sources of High Energy Neutrinos in the IceCube Era*, *Ann. Rev. Nucl. Part. Sci.* **67** (2017) 45–67, [[1708.03577](#)].
- [15] J. Heinze, D. Biehl, A. Fedynitch, D. Boncioli, A. Rudolph and W. Winter, *Systematic parameter space study for the UHECR origin from GRBs in models with multiple internal shocks*, *Mon. Not. Roy. Astron. Soc.* **498** (2020) 5990–6004, [[2006.14301](#)].
- [16] E. Waxman and J. N. Bahcall, *High-energy neutrinos from cosmological gamma-ray burst fireballs*, *Phys. Rev. Lett.* **78** (1997) 2292–2295, [[astro-ph/9701231](#)].

- [17] D. Guetta, D. Hooper, J. Alvarez-Muniz, F. Halzen and E. Reuveni, *Neutrinos from individual gamma-ray bursts in the BATSE catalog*, *Astropart. Phys.* **20** (2004) 429–455, [[astro-ph/0302524](#)].
- [18] K. Wang, R.-Y. Liu, Z.-G. Dai and K. Asano, *Hadronic origin of prompt high-energy emission of gamma-ray bursts revisited: in the case of a limited maximum proton energy*, *Astrophys. J.* **857** (2018) 24, [[1803.04112](#)].
- [19] S. Razzaque, P. Mészáros and E. Waxman, *Neutrino tomography of gamma-ray bursts and massive stellar collapses*, *Phys. Rev. D* **68** (2003) 083001, [[astro-ph/0303505](#)].
- [20] K. Murase and K. Ioka, *TeV–PeV Neutrinos from Low-Power Gamma-Ray Burst Jets inside Stars*, *Phys. Rev. Lett.* **111** (2013) 121102, [[1306.2274](#)].
- [21] B. D. Metzger, D. Giannios and S. Horiuchi, *Heavy Nuclei Synthesized in Gamma-Ray Burst Outflows as the Source of UHECRs*, *Mon. Not. Roy. Astron. Soc.* **415** (2011) 2495, [[1101.4019](#)].
- [22] P. Mészáros, *Gamma Ray Bursts as Neutrino Sources*, [1511.01396](#).
- [23] E. Waxman, *The Origin of IceCube’s Neutrinos: Cosmic Ray Accelerators Embedded in Star Forming Calorimeters*, [1511.00815](#).
- [24] K. Murase, *Active Galactic Nuclei as High-Energy Neutrino Sources*, [1511.01590](#).
- [25] M. Ahlers and F. Halzen, *Opening a New Window onto the Universe with IceCube*, *Prog. Part. Nucl. Phys.* **102** (2018) 73–88, [[1805.11112](#)].
- [26] M. Ahlers and F. Halzen, *High-energy cosmic neutrino puzzle: a review*, *Rept. Prog. Phys.* **78** (2015) 126901.
- [27] ICECUBE collaboration, R. Abbasi et al., *The IceCube high-energy starting event sample: Description and flux characterization with 7.5 years of data*, [2011.03545](#).
- [28] ICECUBE collaboration, R. Abbasi et al., *Measurement of Astrophysical Tau Neutrinos in IceCube’s High-Energy Starting Events*, [2011.03561](#).
- [29] L. A. Anchordoqui et al., *Cosmic Neutrino Pevatrons: A Brand New Pathway to Astronomy, Astrophysics, and Particle Physics*, *JHEAp* **1-2** (2014) 1–30, [[1312.6587](#)].
- [30] E. Vitagliano, I. Tamborra and G. Raffelt, *Grand Unified Neutrino Spectrum at Earth: Sources and Spectral Components*, *Rev. Mod. Phys.* **92** (2020) 45006, [[1910.11878](#)].
- [31] ANTARES collaboration, A. Albert et al., *Constraining the contribution of Gamma-Ray Bursts to the high-energy diffuse neutrino flux with 10 years of ANTARES data*, *Mon. Not. Roy. Astron. Soc.* **500** (2020) 5614–5628, [[2008.02127](#)].
- [32] ICECUBE collaboration, M. Aartsen et al., *Extending the search for muon neutrinos coincident with gamma-ray bursts in IceCube data*, *Astrophys. J.* **843** (2017) 112, [[1702.06868](#)].
- [33] ICECUBE collaboration, M. Aartsen et al., *An All-Sky Search for Three Flavors of Neutrinos from Gamma-Ray Bursts with the IceCube Neutrino Observatory*, *Astrophys. J.* **824** (2016) 115, [[1601.06484](#)].
- [34] Z. Li, *Fermi Limit on the Neutrino Flux from Gamma-Ray Bursts*, *Astrophys. J. Lett.* **770** (2013) L40, [[1210.6594](#)].
- [35] S. Hümmer, P. Baerwald and W. Winter, *Neutrino Emission from Gamma-Ray Burst Fireballs, Revised*, *Phys. Rev. Lett.* **108** (2012) 231101, [[1112.1076](#)].
- [36] I. Tamborra and S. Ando, *Diffuse emission of high-energy neutrinos from gamma-ray burst fireballs*, *JCAP* **09** (2015) 036, [[1504.00107](#)].
- [37] I. Tamborra and S. Ando, *Inspecting the supernova–gamma-ray-burst connection with high-energy neutrinos*, *Phys. Rev. D* **93** (2016) 053010, [[1512.01559](#)].

- [38] M. Bustamante, P. Baerwald, K. Murase and W. Winter, *Neutrino and cosmic-ray emission from multiple internal shocks in gamma-ray bursts*, *Nature Commun.* **6** (2015) 6783, [[1409.2874](#)].
- [39] G. Oganessian, L. Nava, G. Ghirlanda, A. Melandri and A. Celotti, *Prompt optical emission as a signature of synchrotron radiation in gamma-ray bursts*, *Astron. Astrophys.* **628** (2019) A59, [[1904.11086](#)].
- [40] B.-B. Zhang, Z. L. Uhm, V. Connaughton, M. S. Briggs and B. Zhang, *Synchrotron Origin of the Typical GRB Band Function—a Case Study of GRB 130606b*, *Astrophys. J.* **816** (2016) 72, [[1505.05858](#)].
- [41] Z. Acuner, F. Ryde and H.-F. Yu, *Non-dissipative photospheres in GRBs: Spectral appearance in the Fermi/GBM catalogue*, *Mon. Not. Roy. Astron. Soc.* **487** (2019) 5508–5519, [[1906.01318](#)].
- [42] Z. Acuner, F. Ryde, A. Pe’er, D. Mortlock and B. Ahlgren, *The Fraction of Gamma-Ray Bursts with an Observed Photospheric Emission Episode*, *Astrophys. J.* **893** (2020) 128, [[2003.06223](#)].
- [43] J. M. Burgess, D. Bégué, A. Bachelj, D. Giannios, F. Berlato and J. Greiner, *Gamma-ray bursts as cool synchrotron sources*, *Nature Astron.* **4** (2019) 174–179, [[1810.06965](#)].
- [44] M. Rees and P. Mészáros, *Unsteady outflow models for cosmological gamma-ray bursts*, *Astrophys. J. Lett.* **430** (1994) L93–L96, [[astro-ph/9404038](#)].
- [45] K. Toma, X.-F. Wu and P. Mészáros, *A Photosphere-Internal Shock Model of Gamma-Ray Bursts: Case Studies of Fermi/LAT Bursts*, *Mon. Not. Roy. Astron. Soc.* **415** (2011) 1663–1680, [[1002.2634](#)].
- [46] S. Guiriec et al., *Towards a Better Understanding of the GRB Phenomenon: a New Model for GRB Prompt Emission and its effects on the New $L_i^{\text{NT}}-E_{\text{peak},i}^{\text{rest,NT}}$ relation*, *Astrophys. J.* **807** (2015) 148, [[1501.07028](#)].
- [47] B. Zhang and H. Yan, *The Internal-Collision-Induced Magnetic Reconnection and Turbulence (ICMART) Model of Gamma-Ray Bursts*, *Astrophys. J.* **726** (2011) 90, [[1011.1197](#)].
- [48] P. Beniamini and D. Giannios, *Prompt Gamma Ray Burst emission from gradual magnetic dissipation*, *Mon. Not. Roy. Astron. Soc.* **468** (2017) 3202–3211, [[1703.07380](#)].
- [49] R. Gill, J. Granot and P. Beniamini, *GRB Spectrum from Gradual Dissipation in a Magnetized Outflow*, *Mon. Not. Roy. Astron. Soc.* **499** (2020) 1356–1372, [[2008.10729](#)].
- [50] G. Ghisellini, G. Ghirlanda, G. Oganessian, S. Ascenzi, L. Nava, A. Celotti et al., *Proton-synchrotron as the radiation mechanism of the prompt emission of gamma-ray bursts?*, *Astron. Astrophys.* **636** (2020) A82, [[1912.02185](#)].
- [51] I. Florou, M. Petropoulou and A. Mastichiadis, *A marginally fast-cooling proton-synchrotron model for prompt GRBs*, [in preparation](#) (2021).
- [52] O. Bromberg, E. Nakar, T. Piran and R. Sari, *The propagation of relativistic jets in external media*, *Astrophys. J.* **740** (2011) 100, [[1107.1326](#)].
- [53] D. Eichler, M. Livio, T. Piran and D. N. Schramm, *Nucleosynthesis, neutrino bursts and γ -rays from coalescing neutron stars*, *Nature* **340** (July, 1989) 126–128.
- [54] R. Popham, S. E. Woosley and C. Fryer, *Hyperaccreting Black Holes and Gamma-Ray Bursts*, *Astrophys. J.* **518** (June, 1999) 356–374, [[astro-ph/9807028](#)].
- [55] P. Mészáros and M. J. Rees, *Poynting Jets from Black Holes and Cosmological Gamma-Ray Bursts*, *Astrophys. J. Lett.* **482** (June, 1997) L29–L32, [[astro-ph/9609065](#)].
- [56] J. Goodman, *Are gamma-ray bursts optically thick?*, *Astrophys. J. Lett.* **308** (1986) L47–L50.

- [57] T. Piran, A. Shemi and R. Narayan, *Hydrodynamics of relativistic fireballs*, *Mon. Not. Roy. Astron. Soc.* **263** (1993) 861, [[astro-ph/9301004](#)].
- [58] D. Lazzati, B. Morsony, R. Margutti and M. Begelman, *Photospheric emission as the dominant radiation mechanism in long-duration gamma-ray bursts*, *Astrophys. J.* **765** (2013) 103, [[1301.3920](#)].
- [59] C. D. Dermer and G. Menon, *High energy radiation from black holes: Gamma rays, cosmic rays and neutrinos*. Princeton U. Pr., Princeton, USA, 2009.
- [60] P. Mészáros, P. Laguna and M. Rees, *Gas dynamics of relativistically expanding gamma-ray burst sources: Kinematics, energetics, magnetic fields and efficiency*, *Astrophys. J.* **415** (1993) 181–190, [[astro-ph/9301007](#)].
- [61] A. Mizuta and K. Ioka, *Opening Angles of Collapsar Jets*, *Astrophys. J.* **777** (2013) 162, [[1304.0163](#)].
- [62] P. Mészáros and M. Rees, *Steep slopes and preferred breaks in GRB spectra: The Role of photospheres and comptonization*, *Astrophys. J.* **530** (2000) 292–298, [[astro-ph/9908126](#)].
- [63] T. Piran, *Gamma-ray bursts and the fireball model*, *Phys. Rept.* **314** (1999) 575–667, [[astro-ph/9810256](#)].
- [64] H. van Eerten, *Gamma-ray burst afterglow blast waves*, *Int. J. Mod. Phys. D* **27** (2018) 1842002, [[1801.01848](#)].
- [65] A. Panaitescu and P. Kumar, *Analytic light-curves of gamma-ray burst afterglows: homogeneous versus wind external media*, *Astrophys. J.* **543** (2000) 66, [[astro-ph/0003246](#)].
- [66] R. Sari and T. Piran, *Hydrodynamic time scales and temporal structure in GRBs*, *AIP Conf. Proc.* **384** (1996) 782–786, [[astro-ph/9512125](#)].
- [67] R. Blandford and C. McKee, *Fluid dynamics of relativistic blast waves*, *Phys. Fluids* **19** (1976) 1130–1138.
- [68] B. Zhang, *The Physics of Gamma-Ray Bursts*. Cambridge University Press, 12, 2018.
- [69] S. Kobayashi, T. Piran and R. Sari, *Can internal shocks produce the variability in GRBs?*, *Astrophys. J.* **490** (1997) 92–98, [[astro-ph/9705013](#)].
- [70] F. Daigne and R. Mochkovitch, *Gamma-ray bursts from internal shocks in a relativistic wind: temporal and spectral properties*, *Mon. Not. Roy. Astron. Soc.* **296** (1998) 275, [[astro-ph/9801245](#)].
- [71] D. Guetta, M. Spada and E. Waxman, *Efficiency and spectrum of internal gamma-ray burst shocks*, *Astrophys. J.* **557** (2001) 399, [[astro-ph/0011170](#)].
- [72] M. Bustamante, K. Murase, W. Winter and J. Heinze, *Multi-messenger light curves from gamma-ray bursts in the internal shock model*, *Astrophys. J.* **837** (2017) 33, [[1606.02325](#)].
- [73] A. Rudolph, J. Heinze, A. Fedynitch and W. Winter, *Impact of the Collision Model on the Multi-messenger Emission from Gamma-Ray Burst Internal Shocks*, *Astrophys. J.* **893** (2020) 72, [[1907.10633](#)].
- [74] A. Beloborodov and P. Mészáros, *Photospheric Emission of Gamma-Ray Bursts*, *Space Sci. Rev.* **207** (2017) 87–110, [[1701.04523](#)].
- [75] C. Thompson, *A Model of gamma-ray bursts*, *Mon. Not. Roy. Astron. Soc.* **270** (1994) 480.
- [76] D. Giannios, *Prompt emission spectra from the photosphere of a grb*, *Astron. Astrophys.* **457** (2006) 763–770, [[astro-ph/0602397](#)].
- [77] R. Gill and C. Thompson, *Non-thermal Gamma-ray Emission from Delayed Pair Breakdown in a Magnetized and Photon-rich Outflow*, *Astrophys. J.* **796** (2014) 81, [[1406.4774](#)].

- [78] M. Rees and P. Mészáros, *Dissipative photosphere models of gamma-ray bursts and x-ray flashes*, *Astrophys. J.* **628** (2005) 847–852, [[astro-ph/0412702](#)].
- [79] I. Vurm, Y. Lyubarsky and T. Piran, *On thermalization in gamma-ray burst jets and the peak energies of photospheric spectra*, *Astrophys. J.* **764** (2013) 143, [[1209.0763](#)].
- [80] I. Vurm and A. M. Beloborodov, *Radiative Transfer Models for Gamma-Ray Bursts*, *Astrophys. J.* **831** (2016) 175, [[1506.01107](#)].
- [81] A. M. Beloborodov, *Regulation of the spectral peak in gamma-ray bursts*, *Astrophys. J.* **764** (2013) 157, [[1207.2707](#)].
- [82] D. Giannios and H. C. Spruit, *Spectral and timing properties of a dissipative GRB photosphere*, *Astron. Astrophys.* **469** (2007) 1–9, [[astro-ph/0611385](#)].
- [83] C. Thompson and R. Gill, *Hot Electromagnetic Outflows. III. Displaced Fireball in a Strong Magnetic Field*, *Astrophys. J.* **791** (2014) 46, [[1310.2480](#)].
- [84] A. M. Beloborodov, *Collisional mechanism for GRB emission*, *Mon. Not. Roy. Astron. Soc.* **407** (2010) 1033, [[0907.0732](#)].
- [85] D. Lazzati, B. J. Morsony and M. Begelman, *Very high efficiency photospheric emission in long duration gamma-ray bursts*, *Astrophys. J. Lett.* **700** (2009) L47–L50, [[0904.2779](#)].
- [86] O. Gottlieb, A. Levinson and E. Nakar, *High efficiency photospheric emission entailed by formation of a collimation shock in gamma-ray bursts*, *Mon. Not. Roy. Astron. Soc.* **488** (2019) 1416–1426, [[1904.07244](#)].
- [87] J. N. Bahcall and P. Mészáros, *5-GeV to 10-GeV neutrinos from gamma-ray burst fireballs*, *Phys. Rev. Lett.* **85** (2000) 1362–1365, [[hep-ph/0004019](#)].
- [88] K. Kashiyama, K. Murase and P. Mészáros, *Neutron-Proton-Converter Acceleration Mechanism at Subphotospheres of Relativistic Outflows*, *Phys. Rev. Lett.* **111** (2013) 131103, [[1304.1945](#)].
- [89] X.-Y. Wang and Z.-G. Dai, *Prompt TeV neutrinos from dissipative photospheres of gamma-ray bursts*, *Astrophys. J. Lett.* **691** (2009) L67–L71, [[0807.0290](#)].
- [90] K. Murase, *Prompt High-Energy Neutrinos from Gamma-Ray Bursts in the Photospheric and Synchrotron Self-Compton Scenarios*, *Phys. Rev. D* **78** (2008) 101302, [[0807.0919](#)].
- [91] D. Xiao, Z.-G. Dai and P. Mészáros, *Prompt Neutrino Emission of Gamma-Ray Bursts in the Dissipative Photospheric Scenario Revisited: Possible Contributions from Cocoons*, *Astrophys. J.* **843** (2017) 17, [[1706.01293](#)].
- [92] K. Murase, K. Kashiyama and P. Mészáros, *Subphotospheric Neutrinos from Gamma-Ray Bursts: The Role of Neutrons*, *Phys. Rev. Lett.* **111** (2013) 131102, [[1301.4236](#)].
- [93] A. M. Beloborodov, *Sub-photospheric shocks in relativistic explosions*, *Astrophys. J.* **838** (2017) 125, [[1604.02794](#)].
- [94] B. Zhang and B. Zhang, *Gamma-Ray Burst Prompt Emission Light Curves and Power Density Spectra in the ICMART Model*, *Astrophys. J.* **782** (2014) 92, [[1312.7701](#)].
- [95] K. Parfrey, D. Giannios and A. M. Beloborodov, *Black-hole jets without large-scale net magnetic flux*, *Mon. Not. Roy. Astron. Soc.* **446** (2015) L61–L65, [[1410.0374](#)].
- [96] L. Sironi, M. Petropoulou and D. Giannios, *Relativistic jets shine through shocks or magnetic reconnection?*, *Mon. Not. Roy. Astron. Soc.* **450** (2015) 183–191, [[1502.01021](#)].
- [97] F. Guo, X. Li, H. Li, W. Daughton, B. Zhang, N. Lloyd-Ronning et al., *Efficient Production of High-energy Nonthermal Particles During Magnetic Reconnection in a Magnetically Dominated Ion–electron Plasma*, *Astrophys. J. Lett.* **818** (2016) L9, [[1511.01434](#)].

- [98] G. Werner, D. Uzdensky, M. Begelman, B. Cerutti and K. Nalewajko, *Non-thermal particle acceleration in collisionless relativistic electron–proton reconnection*, *Mon. Not. Roy. Astron. Soc.* **473** (2018) 4840–4861, [[1612.04493](#)].
- [99] M. Petropoulou, L. Sironi, A. Spitkovsky and D. Giannios, *Relativistic Magnetic Reconnection in Electron-Positron-Proton Plasmas: Implications for Jets of Active Galactic Nuclei*, *Astrophys. J.* **880** (July, 2019) 37, [[1906.03297](#)].
- [100] L. Sironi and A. Spitkovsky, *Relativistic Reconnection: an Efficient Source of Non-Thermal Particles*, *Astrophys. J. Lett.* **783** (2014) L21, [[1401.5471](#)].
- [101] F. Guo, H. Li, W. Daughton and Y.-H. Liu, *Formation of hard power laws in the energetic particle spectra resulting from relativistic magnetic reconnection*, *Phys. Rev. Lett.* **113** (Oct, 2014) 155005.
- [102] G. R. Werner, D. A. Uzdensky, B. Cerutti, K. Nalewajko and M. C. Begelman, *The Extent of Power-law Energy Spectra in Collisionless Relativistic Magnetic Reconnection in Pair Plasmas*, *Astrophys. J. Lett.* **816** (Jan., 2016) L8, [[1409.8262](#)].
- [103] G. Oganessian, L. Nava, G. Ghirlanda and A. Celotti, *Detection of Low-energy Breaks in Gamma-Ray Burst Prompt Emission Spectra*, *Astrophys. J.* **846** (2017) 137, [[1709.04689](#)].
- [104] M. Ravasio, G. Ghirlanda, L. Nava and G. Ghisellini, *Evidence of two spectral breaks in the prompt emission of gamma ray bursts*, *Astron. Astrophys.* **625** (2019) A60, [[1903.02555](#)].
- [105] F. Daigne, Z. Bosnjak and G. Dubus, *Reconciling observed GRB prompt spectra with synchrotron radiation ?*, *Astron. Astrophys.* **526** (2011) A110, [[1009.2636](#)].
- [106] P. Kumar and R. B. Duran, *On the generation of high energy photons detected by the Fermi Satellite from gamma-ray bursts*, *Mon. Not. Roy. Astron. Soc.* **400** (2009) 75, [[0905.2417](#)].
- [107] R. Santana, R. B. Duran and P. Kumar, *Magnetic Fields In Relativistic Collisionless Shocks*, *Astrophys. J.* **785** (2014) 29, [[1309.3277](#)].
- [108] P. Beniamini, L. Nava and T. Piran, *A revised analysis of gamma-ray bursts’ prompt efficiencies*, *Mon. Not. Roy. Astron. Soc.* **461** (2016) 51–59, [[1606.00311](#)].
- [109] X.-G. Wang et al., *How bad or Good are the External Forward Shock Afterglow Models of Gamma-ray Bursts?*, *Astrophys. J. Suppl.* **219** (2015) 9, [[1503.03193](#)].
- [110] J. L. Racusin et al., *Fermi and Swift Gamma-Ray Burst Afterglow Population Studies*, *Astrophys. J.* **738** (2011) 138, [[1106.2469](#)].
- [111] N. M. Lloyd-Ronning and B. Zhang, *On the kinetic energy and radiative efficiency of gamma-ray bursts*, *Astrophys. J.* **613** (2004) 477–483, [[astro-ph/0404107](#)].
- [112] K. Nalewajko, D. A. Uzdensky, B. Cerutti, G. R. Werner and M. C. Begelman, *On the Distribution of Particle Acceleration Sites in Plasmoid-dominated Relativistic Magnetic Reconnection*, *Astrophys. J.* **815** (Dec., 2015) 101, [[1508.02392](#)].
- [113] M. Petropoulou and L. Sironi, *The steady growth of the high-energy spectral cut-off in relativistic magnetic reconnection*, *Mon. Not. Roy. Astron. Soc.* **481** (2018) 5687–5701, [[1808.00966](#)].
- [114] P. Kilian, X. Li, F. Guo and H. Li, *Exploring the Acceleration Mechanisms for Particle Injection and Power-law Formation during Transrelativistic Magnetic Reconnection*, *Astrophys. J.* **899** (Aug., 2020) 151, [[2001.02732](#)].
- [115] P. Lipari, M. Lusignoli and D. Meloni, *Flavor Composition and Energy Spectrum of Astrophysical Neutrinos*, *Phys. Rev. D* **75** (2007) 123005, [[0704.0718](#)].
- [116] L. Sironi, A. Spitkovsky and J. Arons, *The Maximum Energy of Accelerated Particles in Relativistic Collisionless Shocks*, *Astrophys. J.* **771** (2013) 54, [[1301.5333](#)].

- [117] J. Matthews, A. Bell and K. Blundell, *Particle acceleration in astrophysical jets*, *New Astron. Rev.* **89** (2020) 101543, [[2003.06587](#)].
- [118] S. Hümmel, M. Ruger, F. Spanier and W. Winter, *Simplified models for photohadronic interactions in cosmic accelerators*, *Astrophys. J.* **721** (2010) 630–652, [[1002.1310](#)].
- [119] S. Razzaque, P. Mészáros and E. Waxman, *High energy neutrinos from a slow jet model of core collapse supernovae*, *Mod. Phys. Lett. A* **20** (2005) 2351–2368, [[astro-ph/0509729](#)].
- [120] S. Gao, K. Asano and P. Mészáros, *High Energy Neutrinos from Dissipative Photospheric Models of Gamma Ray Bursts*, *JCAP* **11** (2012) 058, [[1210.1186](#)].
- [121] PARTICLE DATA GROUP collaboration, P. Zyla et al., *Review of Particle Physics*, *PTEP* **2020** (2020) 083C01.
- [122] F. C. Jones, *Inverse Compton Scattering of Cosmic-Ray Electrons*, *Phys. Rev.* **137** (Mar, 1965) B1306–B1311.
- [123] A. Mücke, R. Engel, J. Rachen, R. Protheroe and T. Stanev, *SOPHIA: Monte Carlo simulations of photohadronic processes in astrophysics*, *Comput. Phys. Commun.* **124** (2000) 290–314, [[astro-ph/9903478](#)].
- [124] K. Asano and S. Nagataki, *Very high energy neutrinos originating from kaons in gamma-ray bursts*, *Astrophys. J. Lett.* **640** (2006) L9–L12, [[astro-ph/0603107](#)].
- [125] M. Petropoulou, D. Giannios and S. Dimitrakoudis, *Implications of a PeV neutrino spectral cutoff in GRB models*, *Mon. Not. Roy. Astron. Soc.* **445** (2014) 570–580, [[1405.2091](#)].
- [126] I. Esteban, M. Gonzalez-Garcia, M. Maltoni, T. Schwetz and A. Zhou, *The fate of hints: updated global analysis of three-flavor neutrino oscillations*, *JHEP* **09** (2020) 178, [[2007.14792](#)].
- [127] P. Baerwald, S. Hümmel and W. Winter, *Systematics in the Interpretation of Aggregated Neutrino Flux Limits and Flavor Ratios from Gamma-Ray Bursts*, *Astropart. Phys.* **35** (2012) 508–529, [[1107.5583](#)].
- [128] PLANCK collaboration, N. Aghanim et al., *Planck 2018 results. VI. Cosmological parameters*, *Astron. Astrophys.* **641** (2020) A6, [[1807.06209](#)].
- [129] P. Baerwald, M. Bustamante and W. Winter, *UHECR escape mechanisms for protons and neutrons from GRBs, and the cosmic ray-neutrino connection*, *Astrophys. J.* **768** (2013) 186, [[1301.6163](#)].
- [130] F. Samuelsson, D. Bégué, F. Ryde and A. Pe’er, *The Limited Contribution of Low- and High-Luminosity Gamma-Ray Bursts to Ultra-High Energy Cosmic Rays*, *Astrophys. J.* **876** (2019) 93, [[1810.06579](#)].
- [131] FERMI-LAT collaboration, M. Ajello et al., *Investigating the Nature of Late-time High-energy GRB Emission through Joint Fermi/Swift Observations*, *Astrophys. J.* **863** (2018) 138, [[1808.01683](#)].
- [132] B. Zhang and P. Kumar, *Model-dependent high-energy neutrino flux from Gamma-Ray Bursts*, *Phys. Rev. Lett.* **110** (2013) 121101, [[1210.0647](#)].
- [133] S. Guiriec, C. Kouveliotou, D. Hartmann, J. Granot, K. Asano, P. Mészáros et al., *A Unified Model for GRB Prompt Emission from Optical to γ -Rays; Exploring GRBs as Standard Candle*, *Astrophys. J. Lett.* **831** (2016) L8, [[1606.07193](#)].
- [134] M. Arimoto, K. Asano, M. Ohno, P. Veres, M. Axelsson, E. Bissaldi et al., *High-energy Non-thermal and Thermal Emission From GRB 141207a Detected by Fermi*, *Astrophys. J.* **833** (2016) 139, [[1610.04867](#)].

- [135] P. Beniamini, L. Nava, R. Barniol Duran and T. Piran, *Energies of GRB blast waves and prompt efficiencies as implied by modelling of X-ray and GeV afterglows*, *Mon. Not. Roy. Astron. Soc.* **454** (2015) 1073–1085, [1504.04833].
- [136] S. Razzaque, *Long-lived PeV–EeV neutrinos from gamma-ray burst blastwave*, *Phys. Rev. D* **88** (2013) 103003, [1307.7596].
- [137] M. Ajello et al., *Fermi and Swift Observations of GRB 190114C: Tracing the Evolution of High-Energy Emission from Prompt to Afterglow*, *Astrophys. J.* **890** (2020) 9, [1909.10605].
- [138] W. Deng, H. Li, B. Zhang and S. Li, *Relativistic MHD simulations of collision-induced magnetic dissipation in Poynting-flux-dominated jets/outflows*, *Astrophys. J.* **805** (2015) 163, [1501.07595].
- [139] K. Liu, D.-B. Lin, K. Wang, L. Zhou, X.-G. Wang and E.-W. Liang, *Gamma-ray Burst Spectrum with a Time-dependent Injection Rate of High-energy Electrons*, *Astrophys. J. Lett.* **893** (2020) L14, [2003.12231].
- [140] GRB web catalog, https://icecube.wisc.edu/~grbweb_public/.
- [141] N. Gupta and B. Zhang, *Prompt Emission of High Energy Photons from Gamma Ray Bursts*, *Mon. Not. Roy. Astron. Soc.* **380** (2007) 78, [0704.1329].
- [142] ICECUBE GEN2 collaboration, M. G. Aartsen et al., *IceCube-Gen2: The Window to the Extreme Universe*, 2008.04323.
- [143] KM3NET collaboration, S. Adrian-Martinez et al., *Letter of intent for KM3NeT 2.0*, *J. Phys. G* **43** (2016) 084001, [1601.07459].
- [144] M. Petropoulou, *The role of hadronic cascades in GRB models of efficient neutrino production*, *Mon. Not. Roy. Astron. Soc.* **442** (2014) 3026–3036, [1405.7669].
- [145] M. Petropoulou, S. Dimitrakoudis, A. Mastichiadis and D. Giannios, *Hadronic supercriticality as a trigger for γ -ray burst emission*, *Mon. Not. Roy. Astron. Soc.* **444** (2014) 2186–2199, [1407.2915].
- [146] K. Murase, K. Asano, T. Terasawa and P. Meszaros, *The Role of Stochastic Acceleration in the Prompt Emission of Gamma-Ray Bursts: Application to Hadronic Injection*, *Astrophys. J.* **746** (2012) 164, [1107.5575].
- [147] K. Asano and P. Mészáros, *Photon and Neutrino Spectra of Time-Dependent Photospheric Models of Gamma-Ray Bursts*, *JCAP* **09** (2013) 008, [1308.3563].
- [148] A. Mastichiadis, I. Florou, E. Kefala, S. S. Boula and M. Petropoulou, *A roadmap to hadronic supercriticalities: a comprehensive study of the parameter space for high-energy astrophysical sources*, *Mon. Not. Roy. Astron. Soc.* **495** (2020) 2458–2474, [2003.06956].
- [149] D. Band et al., *BATSE observations of gamma-ray burst spectra. 1. Spectral diversity*, *Astrophys. J.* **413** (1993) 281–292.
- [150] L. Amati, *The $E(p,i)$ - $E(iso)$ correlation in grbs: updated observational status, re-analysis and main implications*, *Mon. Not. Roy. Astron. Soc.* **372** (2006) 233–245, [astro-ph/0601553].
- [151] H.-F. Yu et al., *The Fermi GBM gamma-ray burst time-resolved spectral catalog: brightest bursts in the first four years*, *Astron. Astrophys.* **588** (2016) A135, [1601.05206].
- [152] H.-F. Yu, H. Dereli-Bégué and F. Ryde, *Bayesian Time-Resolved Spectroscopy of GRB Pulses*, 1810.07313.
- [153] K. Asano and T. Terasawa, *Stochastic Acceleration Model of Gamma-Ray Burst with Decaying Turbulence*, *Mon. Not. Roy. Astron. Soc.* **454** (2015) 2242–2248, [1509.04477].
- [154] T. Sakamoto et al., *The First Swift BAT Gamma-Ray Burst Catalog*, *Astrophys. J. Suppl.* **175** (2008) 179–190, [0707.4626].